Mars atmospheric CO[subscript 2] condensation above the north and south poles as revealed by radio occultation, climate sounder, and laser ranging observations

Mars atmospheric CO_2 condensation above the north and south poles as revealed by radio occultation, climate sounder, and laser ranging observations

Renyu Hu,[1] Kerri Cahoy,[1,2] and Maria T. Zuber[1]

Received 26 March 2012; revised 24 May 2012; accepted 25 May 2012; published 10 July 2012.

[1] We study the condensation of CO_2 in Mars' atmosphere using temperature profiles retrieved from radio occultation measurements from Mars Global Surveyor (MGS) as well as the climate sounding instrument onboard the Mars Reconnaissance Orbiter (MRO), and detection of reflective clouds by the MGS Mars Orbiter Laser Altimeter (MOLA). We find 11 events in 1999 where MGS temperature profiles indicate CO_2 condensation and MOLA simultaneously detects reflective clouds. We thus provide causal evidence that MOLA non-ground returns are associated with CO_2 condensation, which strongly indicates their nature being CO_2 clouds. The MGS and MRO temperature profiles together reveal the seasonal expansion and shrinking of the area and the vertical extent of atmospheric saturation. The occurrence rate of atmospheric saturation is maximized at high latitudes in the middle of winter. The atmospheric saturation in the northern polar region exhibits more intense seasonal variation than in the southern polar region. In particular, a shrinking of saturation area and thickness from $L_S \sim 270^\circ$ to $\sim 300^\circ$ in 2007 is found; this is probably related to a planet-encircling dust storm. Furthermore, we integrate the condensation area and the condensation occurrence rate to estimate cumulative masses of CO_2 condensates deposited onto the northern and southern seasonal polar caps. The precipitation flux is approximated by the particle settling flux which is estimated using the impulse responses of MOLA filter channels. With our approach, the total atmospheric condensation mass can be estimated from these observational data sets with average particle size as the only free parameter. By comparison with the seasonal polar cap masses inferred from the time-varying gravity of Mars, our estimates indicate that the average condensate particle radius is 8–22 μm in the northern hemisphere and 4–13 μm in the southern hemisphere. Our multi-instrument data analysis provides new constraints on modeling the global climate of Mars.

Citation: Hu, R., K. Cahoy, and M. T. Zuber (2012), Mars atmospheric CO_2 condensation above the north and south poles as revealed by radio occultation, climate sounder, and laser ranging observations, *J. Geophys. Res.*, *117*, E07002, doi:10.1029/2012JE004087.

1. Introduction

1.1. CO_2 Cycle Background

[2] Seasonal CO_2 cycle is one of the dominant drivers of the global climate on Mars. Condensation and deposition of a significant percentage of atmospheric mass on Mars' poles and a seasonal variation of atmospheric pressure were first proposed by *Leighton and Murray* [1966] and confirmed by the Viking landers [*Hess et al.*, 1979; *Tillman et al.*, 1993]. The condensation and deposition of CO_2 onto the polar regions during fall and winter lead to the formation of seasonal polar caps, whose spatial extent, thickness, and mass exhibit prominent seasonal variations. The seasonal polar caps extend to latitudes of $\pm 50^\circ$ in the middle of polar winter, derived from the observations of the Thermal Emission Spectrometer (TES) onboard the Mars Global Surveyor (MGS) spacecraft [*Kieffer et al.*, 2000; *Kieffer and Titus*, 2001]. The TES polar cap sizes are also confirmed by observations from the Mars Express spacecraft [e.g., *Langevin et al.*, 2007].

[3] Seasonal variation of the height of Mars polar caps has been measured by the Mars Orbiter Laser Altimeter (MOLA) [*Zuber et al.*, 1992; *Smith et al.*, 2001a, 2001b] on MGS. At high latitudes (poleward of 80°) the surface elevation can change by more than 1 m over the course of a Martian year due to the deposition of CO_2 snow [*Smith et al.*, 2001a]. The laser altimeter observations thus capture the seasonal cycle of carbon dioxide mass exchange between the Martian surface and atmosphere. Beneath the seasonal cap, the residual south

[1]Department of Earth, Atmospheric and Planetary Sciences, Massachusetts Institute of Technology, Cambridge, Massachusetts, USA.
[2]NASA Goddard Space Flight Center, Greenbelt, Maryland, USA.

Corresponding author: R. Hu, Department of Earth, Atmospheric and Planetary Sciences, Massachusetts Institute of Technology, 54-1719, 77 Massachusetts Ave., Cambridge, MA 02139-4307, USA. (hury@mit.edu)

0148-0227/12/2012JE004087

polar cap, which consists primarily of H_2O ice, survives the southern summer on Mars. The residual cap includes a thin ($\sim$1–2 m) surficial CO_2 ice layer that represents less than 3% of the total mass of the current Mars atmosphere [e.g., *Thomas et al.*, 2009].

[4] *Smith et al.* [2009b] presented evidence for time-variation of Mars' gravitational field over four Mars years (MY), measured by the Doppler tracking [*Tyler et al.*, 1992] of MGS. Mars years are numbered according to the calendar proposed by *Clancy et al.* [2000]: Mars Year 1 begins on April 11, 1955 ($L_S = 0°$). The seasonal CO_2 masses of north polar cap, south polar cap, and atmosphere, retrieved from the measurement of small temporal changes in gravity, generally agree with the simulated atmospheric mass exchange from the Ames General Circulation Model [*Pollack et al.*, 1990, 1993]. From *Smith et al.* [2009b], the seasonal north polar cap reaches the maximum mass of $\sim 4 \times 10^{18}$ g at $L_S \sim 360°$, and the seasonal south polar cap reaches the maximum mass of $\sim 6 \times 10^{18}$ g at $L_S \sim 150°$. The mass of seasonal polar caps has also been inferred from the measurements of neutron flux from Mars [*Litvak et al.*, 2005, 2007], and is in agreement with *Smith et al.* [2009b].

[5] The formation of seasonal polar caps involves two separate physical processes: surface direct deposition and atmospheric precipitation. Surface direct deposition, originally proposed by *Leighton and Murray* [1966], has been suggested to be a major process that accounts for the mass accumulation on the seasonal caps [*Pollack et al.*, 1990; *Forget et al.*, 1998; *Colaprete et al.*, 2005, 2008]. Surface energy balance models have been developed to estimate the mass of seasonal polar caps and explain the variation of atmospheric pressure [e.g., *Pollack et al.*, 1993; *Wood and Paige*, 1992]. The picture of surface direct deposition is complicated by a number of variable factors, including the surface thermal inertia, surface emissivity, contamination of dust and water ices, etc. [*Kieffer and Titus*, 2001; *Putzig and Mellon*, 2007; *Haberle et al.*, 2008].

1.2. CO_2 Condensation and Precipitation

[6] Atmospheric condensation and precipitation of CO_2 condensates also contributes to the formation of seasonal polar caps [*Pollack et al.*, 1990; *Forget et al.*, 1998; *Colaprete et al.*, 2005, 2008]. Three observational measurements of atmospheric condensation and precipitation on Mars are the presence of atmospheric saturation, reflective clouds in the atmosphere, and cold spots on the surface.

[7] First, condensation of CO_2 requires that the atmosphere becomes supersaturated, i.e. that the temperature at a certain pressure level of the atmosphere falls below the CO_2 saturation curve. The MGS Radio Science (RS) investigation [*Tyler et al.*, 1992, 2001] measured the temperature-pressure profiles of Mars' atmosphere using the radio occultation technique, and found atmospheric saturation in polar nights [*Hinson et al.*, 1999; *Colaprete et al.*, 2003]. The TES instrument on MGS also retrieved temperature profiles and found atmospheric saturation during polar nights [*Conrath et al.*, 2000; *Colaprete et al.*, 2008].

[8] Second, CO_2 condensates in the atmosphere have been observed by MOLA as non-ground returns. MOLA is a laser-ranging instrument which measured surface topography, roughness, and albedo at 1.064 μm [*Zuber et al.*, 1992]. During mapping operations, MOLA also obtained nearly 600,000 non-ground returns of elevation up to 20 km [*Zuber et al.*, 1998; *Neumann et al.*, 2003]. The MOLA detector has 4 filter channels that have impulse responses of 20, 60, 180 and 540 ns, which correspond to target dispersions within the laser footprint of 3, 9, 27 and 81 m, respectively.

[9] Third, "cold spots", defined as the location that exhibits infrared (20-μm) brightness temperature significantly lower than the frost temperature of CO_2, have been found in great numbers on the surface of Mars' polar regions in winter [*Kieffer et al.*, 1976; *Titus et al.*, 2001]. These cold spots have been interpreted as fresh CO_2 snow from atmospheric condensation and precipitation [*Hunt*, 1980; *Forget et al.*, 1995; *Forget and Pollack*, 1996; *Hansen*, 1999; *Titus et al.*, 2001; *Ivanov and Muhleman*, 2001; *Cornwall and Titus*, 2009, 2010]. *Ivanov and Muhleman* [2001] reported putative association between MOLA cloud detections and TES cold spots, an evidence that MOLA non-ground returns are CO_2 snow.

[10] The seasonal mass exchange of Mars' surface and atmosphere has been firmly established by seasonal observations of Mars' surface and atmosphere, however, several critical aspects of the atmospheric processes of condensation and deposition remain to be explored by data. Notably, the causality of atmospheric CO_2 condensates is not yet established, the spatial extent of atmospheric saturation has not been directly measured, and the mass of atmospheric CO_2 condensation is unknown. In this paper, we focus on the atmospheric condensation and precipitation of CO_2 in the polar regions of Mars.

1.3. Approach

[11] We simultaneously analyze data from three different Mars orbital experiments, including laser ranging, radio occultation, and climate sounding. We address the cause of condensation of CO_2, and estimate the mass that could condense and be deposited to form the seasonal polar caps. We also compare the mass estimates with a part of the seasonal polar mass inferred from the variation in Mars' gravity field [*Smith et al.*, 2001b], and provide constraints on the size of condensate particles.

[12] We use MOLA non-ground returns to probe the properties of CO_2 clouds. The MOLA non-ground returns indicate reflective particles in the Martian atmosphere, and the triggering channels contain information on the cloud opacity and particle concentration. For example, in order to trigger a return in Channel 1, the optical depth along the line of sight at the MOLA wavelength should increase from zero to 1 in $\sim$3 m [e.g., *Neumann et al.*, 2003]. As a result, the MOLA non-ground returns not only provide information about the altitude and the distribution of clouds, but also the concentration of CO_2 condensate particles in the Martian atmosphere.

[13] We use the temperature profiles measured by the MGS RS investigation and the Mars Climate Sounder (MCS) [*McCleese et al.*, 2007] onboard the Mars Reconnaissance Orbiter (MRO) [*Zurek and Smrekar*, 2007] to synthesize the spatial extent of atmospheric saturation on Mars. The MGS RS temperature profile measurements span 6 Mars years and provide an opportunity to investigate interannual variability [e.g., *Tyler et al.*, 2001], and the MCS temperature profile measurements densely and consistently cover the Mars polar regions and allow statistical study of the phenomena

Table 1. MOLA Cloud Triggers by Filter Channels[a]

Channel	Impulse Response	MY 24	MY 25	Total
1	20 ns	84407	159	84566
2	60 ns	64040	31603	95643
3	180 ns	112140	34543	146683
4	540 ns	173953	45030	218983

[a]MOLA detects cloud returns during $L_S \sim 103°$–$360°$ in MY 24 and $L_S \sim 0°$–$188°$ in MY 25.

[*McCleese et al.*, 2007, 2010]. The two data sets are also complimentary in terms of their time of operation.

[14] In this paper, we compare the MOLA non-ground returns with temperature profiles derived from MGS radio occultations, and use the temperature profiles of MGS RS and MCS to reveal the seasonal behavior of atmospheric condensation in terms of area and vertical range. Finally, we estimate the mass of CO_2 deposited onto the seasonal polar caps, and compare our results with the time-variation of Mars' gravity field. In § 2 we present a brief summary of the data. In § 3 we present the results of the data analysis, including the association of MOLA clouds and atmospheric saturation, the spatial extent of atmospheric saturation, and the estimates of mass of condensation and precipitation. In § 4 we discuss on the cloud formation in Mars' atmosphere and the size of CO_2 condensate particles. Our final summary is in § 5.

2. Data Summary

2.1. MGS MOLA

[15] During the MGS mapping mission, MOLA accumulated 545,875 non-ground returns from $L_S \sim 103°$ in MY 24 to $L_S \sim 188°$ in MY 25 (G. Neumann, private communication). Numbers of cloud triggers in each filter channel are tabulated in Table 1. Channel 4, the broadest filter, detected the largest number of non-ground returns.

2.2. MGS RS

[16] The MGS RS investigation determines the atmospheric density as a function of altitude by measuring the change in frequency of the ultra-stable radio signal when the MGS spacecraft passes behind Mars such that the radio ray passes through Mars' atmosphere. A temperature-pressure profile can be derived from the density profile assuming hydrostatic equilibrium. The uncertainty of temperature measurements from MGS RS can be as low as 0.4 K at the surface and ~10 K at altitude of 40–50 km [*Hinson et al.*, 1999; *Tyler et al.*, 2001], with a vertical resolution up to 0.5–1 km [*Tyler et al.*, 2001].

[17] From 1998 to 2006, the MGS spacecraft retrieved 21,243 temperature profiles of the Martian atmosphere from the radio occultation experiment. In this work, we concentrate on temperature profiles above the polar caps. The polar cap size model, derived from TES bolometer observations, suggests the seasonal polar cap may extend to latitudes of $\pm 50°$ [*Kieffer et al.*, 2000; *Kieffer and Titus*, 2001; *Smith et al.*, 2009b]. MGS RS measured 12,908 profiles at latitudes between 50.03° and 85.24° in the northern hemisphere, and 3198 profiles at latitudes between −50.02° and −89.84° in the southern hemisphere. Data from the MGS RS investigation have a span of 6 Mars years, from MY 23 to MY 28. We summarize the number of radio occultation temperature profiles at latitudes > 50° in both hemispheres for each Mars year in Table 2. MGS RS measured three times more temperature profiles above the northern polar cap than it did above the southern polar cap.

[18] As seen in Table 2, MGS radio occultation profiles provided extensive coverage of the northern and the southern polar caps during the respective winter seasons in MY 27. For the northern hemisphere, MGS RS provided full coverage of the polar cap during the winter of MY 27, for $L_S \sim 200°$–$355°$, and Lat ~ 61°–80°. In MY 24, 25, and 26, MGS RS partially sampled the polar cap in winter and had limited latitudinal coverage. For the southern hemisphere, MGS RS provided full coverage of the polar cap during the winter of MY 27, for $L_S \sim 22°$–$168°$, and Lat ~ 50°–79°. In MY 24 and 28, MGS RS partially sampled the polar cap in winter and also had limited latitudinal coverage (see Table 2).

2.3. MRO MCS

[19] Subsequent to the MGS mission, the MCS instrument onboard the MRO spacecraft began mapping Mars. The MCS measures the broad-band infrared spectra of Mars' atmosphere in the limb and nadir observations. Vertical profiles of temperature, dust and aerosols can be retrieved from the broad-band spectra. Data from the MCS instrument helps to constrain the lower atmospheric circulation and the forcing of the circulation by radiative heating/cooling due to dust and water ice [*McCleese et al.*, 2010; *Heavens et al.*, 2011].

[20] From September 24, 2006 to January 31, 2011, the MCS instrument onboard MRO accumulated 2,510,668 temperature-pressure profiles, covering MY 28 from $L_S \sim 111°$, most of MY 29 to $L_S \sim 328°$ and the first half of MY 30 to $L_S \sim 228°$. The number of temperature profiles retrieved from MCS measurements in different Mars years and in the L_S and latitude ranges of interest are tabulated in Table 3.

[21] MCS provides temperature measurements that consistently cover the polar caps during the northern hemisphere

Table 2. Summary of the MGS Radio Science Temperature Profiles Above Mars' Polar Caps[a]

Mars Year	23	24	25	26	27	28	Total
No. Profiles > 50°N	0	1287	3403	4105	4113	0	12908
L_S Coverage	NA	267°–360°	305°–360°	200°–270°	200°–355°	NA	
N Latitude Coverage	NA	55°–74°	62°–66°	61°–69°	61°–80°	NA	
No. Profiles > 50°S	40	503	285	84	1325	961	3198
L_S Coverage	NA	108°–161°	NA	NA	22°–168°	51°–109°	
S Latitude Coverage	NA	67°–75°	NA	NA	50°–79°	56°–70°	
Total	40	1790	3688	4189	5438	961	16106

[a]The L_S and latitude coverage is shown only for the Mars years in which the number of profiles is larger than 500. The L_S and latitude coverage includes only the profiles in northern hemisphere and the southern hemisphere "winters", defined as $L_S \sim 200°$–$360°$ and $L_S \sim 0°$–$170°$, respectively.

Table 3. Summary of MRO Climate Sounding Temperature Profiles[a]

Mars Year	28	28	28	29	29	29	29	30	30	30
L_S	111°–180°	180°–270°	270°–360°	0°–90°	90°–180°	180°–270°	270°–328°	23°–90°	90°–180°	180°–228°
N Lat 50°–60°	9067	26312	13498	27401	21355	11692	9704	7192	24492	6768
N Lat 60°–70°	9744	18822	6974	25072	21342	5763	4381	6844	22909	2650
N Lat 70°–80°	10380	22715	3834	24414	21903	1433	1596	7167	24845	2480
N Lat 80°–90°	13507	36546	13077	22584	20449	8294	9423	6911	22759	4198
S Lat 50°–60°	8030	24169	12393	26763	18740	12431	10571	6571	19885	9135
S Lat 60°–70°	7556	26934	12484	26323	15408	12822	9206	6410	20103	8205
S Lat 70°–80°	7482	27905	12479	26607	20452	14522	9983	6098	22937	9077
S Lat 80°–90°	7680	24481	11086	26654	22739	16108	9249	6912	23546	7979

[a]The number of temperature profiles measured in different Mars years and in the L_S and latitude ranges of interest are tabulated. There is a data gap from $L_S \sim 328°$ of MY 29 to $L_S \sim 23°$ of MY 30.

winter of MY 28 and the southern hemisphere winter of MY 29. As seen in Table 3, there are a large number of measurements of the polar atmosphere during these two winters. The measurements are generally uniform with latitude and L_S. In particular, the southern polar cap during the winter of MY 29 is very well sampled by MCS, with more than 40,000 measurements in each latitude range. We note that the number of successful temperature profile retrievals is significantly reduced for the latitudes ranging from 60° to 80° in the northern hemisphere during fall and winter of MY 28 and MY 29, probably due to heavy aerosol loading in the atmosphere [*Kleinböhl et al.*, 2009].

3. Data Analysis and Results

3.1. Association of MOLA Cloud Detection and Atmosphere Supersaturation

[22] MOLA detected non-ground returns in MY 24 and MY 25; at the same time, the radio occultation experiments were also conducted on MGS, the same spacecraft that hosted MOLA. The radio occultation experiment measured atmospheric temperature-pressure profiles on Mars. We present 11 cases during the southern winter of MY 24 in which RS temperature profiles indicated a saturated atmosphere and MOLA concurrently detected a collection of non-ground returns at the same geographic location. The association proves the interpretation that MOLA reflective non-ground returns are due to CO_2 clouds [e.g., *Zuber et al.*, 1998; *Ivanov and Muhleman*, 2001; *Neumann et al.*, 2003], and opens up a new way to study the relation between supersaturation and precipitation. We will begin with a general description of supersaturation observed by radio occultation, followed by the results from the associated events, and an estimate of the concentration of CO_2 condensate particles.

3.1.1. MGS RS Temperature Profiles

[23] Temperature profiles measured by the MGS Radio Science (RS) investigation are compared with the CO_2 saturation curve. MGS RS provides accurate measurements of temperature profiles of the lower atmosphere of Mars. Despite considerable variability, Mars' atmosphere can generally be divided into the lower atmosphere (up to 45 km from the ground), the middle atmosphere (45–110 km), and the upper atmosphere (above 110 km) [*Zurek*, 1992]. Without considering the condensation of CO_2, the lower atmosphere is mainly heated by infrared radiation from the surface, and the temperature profile should follow the moist adiabatic lapse rate of about 4.5 K km^{-1} [*Zurek*, 1992] (see Appendix A for the CO_2 saturation pressure and the moist adiabatic lapse rate). When condensation of CO_2 occurs, the temperature structure becomes more complicated, featuring a layer in the lower atmosphere in which the temperature stays below the condensation temperature. In the following, we refer to this layer as the "condensation layer".

[24] Several MGS RS temperature profiles show a CO_2 condensation layer. Out of 12,908 MGS RS temperature profiles measured above the northern polar cap (Lat > 50°N), 553 profiles contain pressure levels where the atmosphere is saturated. We checked solar zenith angles of the profiles that indicate condensation, and found that they all occur at nighttime (i.e., both diurnal night and polar night). Similarly, out of 3,198 temperature profiles above the southern polar cap (Lat > 50°S), 813 profiles have pressure levels at which the atmosphere is saturated. Note that in this comparison, we took into account the 1-σ measurement uncertainty of temperature and pressure by using the lower limit value of temperature and upper limit value of pressure.

[25] A number of MGS RS temperature profiles show an additional surface layer beneath the condensation layer, in which the temperature is above the condensation temperature and the atmosphere is not saturated. Above the northern polar cap, 149 out of 553 temperature profiles exhibit this surface layer; and above the southern polar cap, 166 out of 813 temperature profiles have such a layer. Figure 1 shows temperature-pressure profiles from the 149 measurements in the northern hemisphere and the 166 measurements in the southern hemisphere, compared with the CO_2 saturation curve and the moist adiabatic lapse rate of the Martian atmosphere.

[26] Three key aspects illustrated by Figure 1:

[27] First, the RS temperature profiles follow the CO_2 saturation curve in the condensation layer. As shown in Figure 1, the difference between the atmospheric temperature and the condensation temperature is generally 1 to 3 K. At a temperature of 140 K, this supercooling temperature corresponds to a saturation ratio of 1.1 to 1.6, or a supersaturation of 10% to 60%. Using all MGS RS temperature profiles that indicate supersaturation, we find that in the northern hemisphere the mean supersaturation is 25% with a standard deviation of 13%, and in the southern hemisphere the mean supersaturation is 30% with a standard deviation of 18%. The maximum supersaturation is 100% in the northern hemisphere and 120% in the southern hemisphere. We did not find any seasonal or latitudinal dependency for the supersaturation. Similar ratios of atmospheric supersaturation have been measured by nadir observations of MGS TES [e.g., *Conrath et al.*, 2000; *Colaprete et al.*, 2008]. The critical saturation

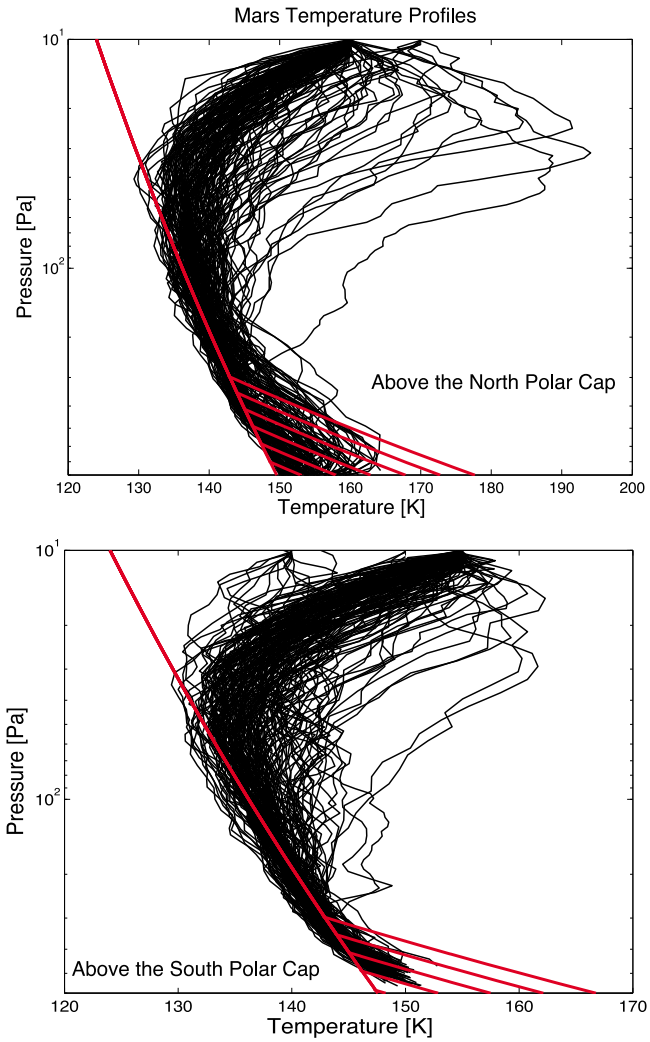

Figure 1. Temperature-pressure profiles above Mars' polar caps measured by MGS radio occultations. Plotted with black curves are 149 profiles above the northern polar cap and 166 profiles above the southern polar cap. For comparison, the CO_2 saturation pressure computed from equations (A1)–(A2) is shown by the upper red curve, and the lower red curves show several temperature profiles that follow the moist adiabatic lapse rate (equation (A3)).

ratio for heterogenous nucleation of CO_2 on water ice is measured to be 1.34 [*Glandorf et al.*, 2002]. The ranges of atmospheric supersaturation observed are consistent with the contact parameter measured by *Glandorf et al.* [2002] and the ranges may correspond to different sizes of ice nuclei due to the curvature effect, or the temperature dependency of critical supersaturation recently reported [*Iraci et al.*, 2010]. The supersaturation measured by MGS radio occultation, therefore, is sufficient for condensation of CO_2.

[28] The RS temperature profiles also indicate that the condensation of CO_2 effectively keeps the atmospheric temperature right below the condensation temperature by releasing the appropriate latent heat. As the temperature gradient of the CO_2 saturation curve is shallower than the adiabatic lapse rate of Mars' atmosphere, the condensation layer is not convective. However, as CO_2 is the major component in Mars' atmosphere, if condensation occurs, the release of latent heat warms up the air parcel with respect to the ambient atmosphere and makes it buoyant [*Colaprete et al.*, 2003, 2008].

[29] Second, below the condensation layer, the temperature-pressure profiles may deviate from the CO_2 saturation curve. As seen in Figure 1, the temperature profiles below the condensation layer generally follow the moist adiabatic lapse rate in the southern hemisphere, suggesting a convective nature for the bottom layer. However, in the northern hemisphere, the temperature gradient below the condensation layer is generally shallower than the moist adiabatic lapse rate. In some cases, near-surface temperatures even turn around and approach the saturation temperature, i.e., a temperature inversion (see Figure 1, top). This feature may indicate the presence of CO_2 ice on the surface. Near-surface temperatures may be warmed by atmospheric circulation, while the surface is still covered by CO_2 ice. The sublimation of CO_2 cools the near-surface temperatures and creates the apparent temperature inversion. We confirm with the MGS RS data that significant near-surface temperature inversion occurred during $L_S \sim 320°$–$360°$, or the spring of the northern hemisphere when CO_2 sublimation is expected.

[30] Third, above the condensation layer, the temperature generally increases with altitude, i.e., the temperature inversion. The temperature inversion in the polar atmosphere above the condensation layer is a phenomenon of atmospheric circulation [e.g., *Pollack et al.*, 1990; *Forget et al.*, 1998]. One might consider that dust, water ice particles, and CO_2 molecules absorb radiative energy from sunlight that heats the middle layer of the atmosphere. However, during the polar night the effect of dust and water ice particles is cooling rather than heating. We define the minimum-temperature pressure (MTP) as the pressure level where the temperature gradient becomes negative, and compare the MTP with the lowest CO_2 condensation pressure in Figure 2.

[31] The MTP correlates with the lowest pressure level where CO_2 condenses. Two populations are evident in Figure 2. The population along the red line in Figure 2 indicates the lowest CO_2 condensation pressure that tracks the MTP. For these cases, atmospheric circulation lifts the temperature above the condensation temperature. As a result, the MTP indicates the highest altitude where CO_2 condensation can happen. A second population exists if the MTP is smaller than 100 Pa, indicating that the lowest CO_2 condensation pressures are larger than the MTP. In that case, the temperature still decreases with altitude while remaining above the condensation temperature. In summary, the lowest CO_2 condensation pressure is found to be equal to or smaller than the MTP.

3.1.2. MOLA Clouds

[32] In this section, we associate the MOLA cloud returns with condensation of CO_2. As shown in Figure 3, we run a thorough check for all the temperature profiles that indicate condensation of CO_2 measured by MGS radio occultation to see if there are associated MOLA cloud detections. The criteria for association are set to be a 2° box of latitude, longitude and L_S, centered on the location of occultation. This criteria is chosen because 1° in latitude or longitude on Mars at the equator corresponds to a distance of about 60 km, which is compatible with sensible horizontal sizes of clouds. The horizontal extent of clouds on Mars is highly variable,

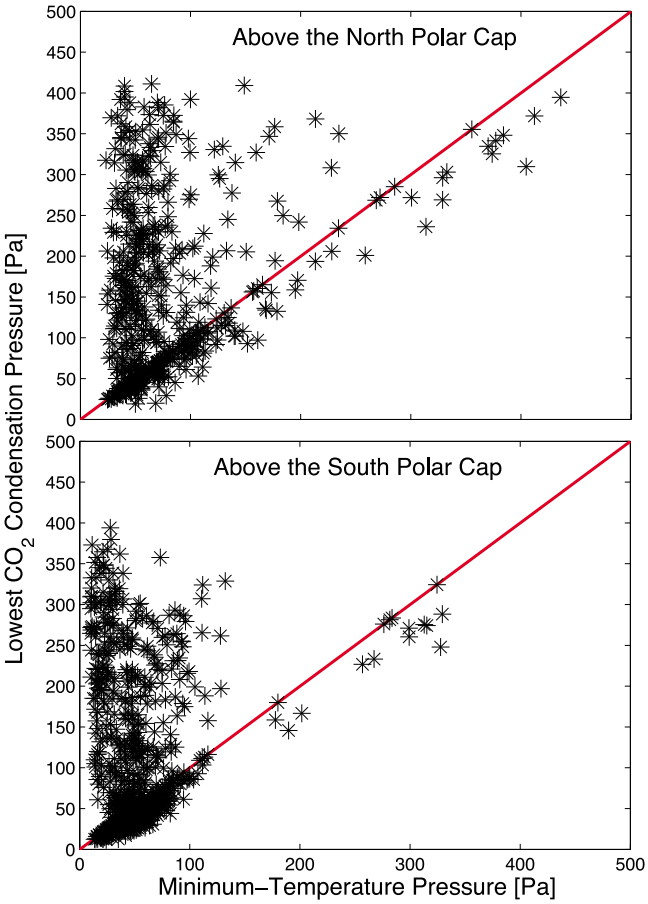

Figure 2. Comparison between the minimum-temperature pressure and the lowest CO_2 condensation pressure, for Mars' temperature profiles above the northern and the southern polar caps, as measured by MGS radio occultations. The red line indicates where the two pressures are equal.

and can be as large as 10 degrees in latitude [*Ivanov and Muhleman*, 2001].

[33] We find 11 temperature profiles below CO_2 saturation measured by MGS RS from 1999 May 9 to 1999 June 13 (MY 24) associated with MOLA cloud detections above the southern polar cap. In this period, both MOLA and RS were operating onboard MGS, and the association implies not only proximity in geographic location and season, but also occurrence at the same time. The geographic locations of these events are shown in Figure 3, and 4 typical association events are presented in Figure 4. We see that each radio occultation profile corresponds to multiple non-ground returns from different channels, which indicates detection of clouds [*Neumann et al.*, 2003]. Furthermore, because the lifetime of the MGS RS experiment is much longer than MOLA, more geographically associated events can be found if we do not require that the MGS RS temperature profiles are measured in the same Mars year as the MOLA detections. We find 44 "weak" association events in this way, with 8 temperature profiles in the northern hemisphere and 36 temperature profiles in the southern hemisphere. We confirm that all of these temperature profiles are above the polar cap during the winter night.

[34] The apparent patchy distribution in Figure 3 may indicate several separate groups of clouds at latitudes of near 70°. Or, the distribution may simply be a geometric effect. Because the geometry of MOLA observations is nadir and the geometry of radio occultation observations is limb, the spacecraft trajectory has to be along the line of sight to produce the associations presented in Figure 3. To better illustrate this, we plot the overall distribution of all MOLA non-ground returns during the same period in Figure 3 (bottom). We find that during the southern hemisphere winter of MY 24, at latitudes about −70°, the cloud hits are most dense in two longitude ranges, 150°∼230° and 310°∼50°. These areas may correspond to two zonal bands of clouds in the southern hemisphere. We note that these longitude ranges also agree with the grouping in Figure 3 (top). The longitude dependence of MOLA clouds is consistent with the general circulation model of Mars' atmosphere considering topographic forcing [*Colaprete et al.*, 2005].

[35] *Colaprete et al.* [2003] introduced the concept of convective available potential energy (CAPE) to describe the convection driven by release of latent heat from CO_2 condensation on Mars. The CAPE, originally a concept in terrestrial meteorology, is defined for Mars' atmosphere as

$$\mathrm{CAPE} = \int_{z_1}^{z_2} g \frac{T_p - T_e}{T_e} dz, \qquad (1)$$

where g is the gravitational acceleration, T_p is the saturation temperature of CO_2, T_e is the actual atmospheric temperature, and z_1 and z_2 define the vertical range of atmospheric CO_2 condensation. The values of CAPE for the typical association events are shown in Figure 4.

[36] As seen in Figure 4, the highest clouds are always found to be lower than the maximum local altitude of CO_2 condensation determined from the radio occultation temperature profiles. This is consistent with the interpretation of MOLA non-ground returns coming from CO_2 condensate clouds. Sometimes CO_2 condensate particles are detected just below the maximum altitude of condensation, such as in Figure 4 (bottom right). Sometimes the highest clouds are detected in the middle of the CO_2 condensation layer, such as in Figure 4 (top left and top right). Moreover, CO_2 condensate particles are often detected near the bottom of the condensation layer, such as in Figure 4 (top left), or even very close to the ground, such as in Figure 4 (bottom left and bottom right). It is unclear how these "low" or "surficial" clouds form. We find that when these near-surface clouds are detected, the CAPE values indicated by the associated temperature profiles are generally less than 50 J kg^{-1}. In general, the altitudes of clouds detected by MOLA are highly variable inside the condensation layer.

3.1.3. Mass of Condensate Particles

[37] The impulse responses of the MOLA filter channels provide information on the optical depth of detected clouds, which can be used to estimate the mass of CO_2 condensate particles per unit volume. This quantity is termed "mass" in order to be distinguished from "density of CO_2 condensates", which means the density of the dry ice solid material. To trigger a return in Channel 1, the cloud optical depth at the MOLA wavelength ($\lambda \sim 1.064$ μm) should increase from zero to about 1 in ∼3 m [*Ivanov and Muhleman*, 2001; *Neumann et al.*, 2003; *Colaprete et al.*, 2003]. In other

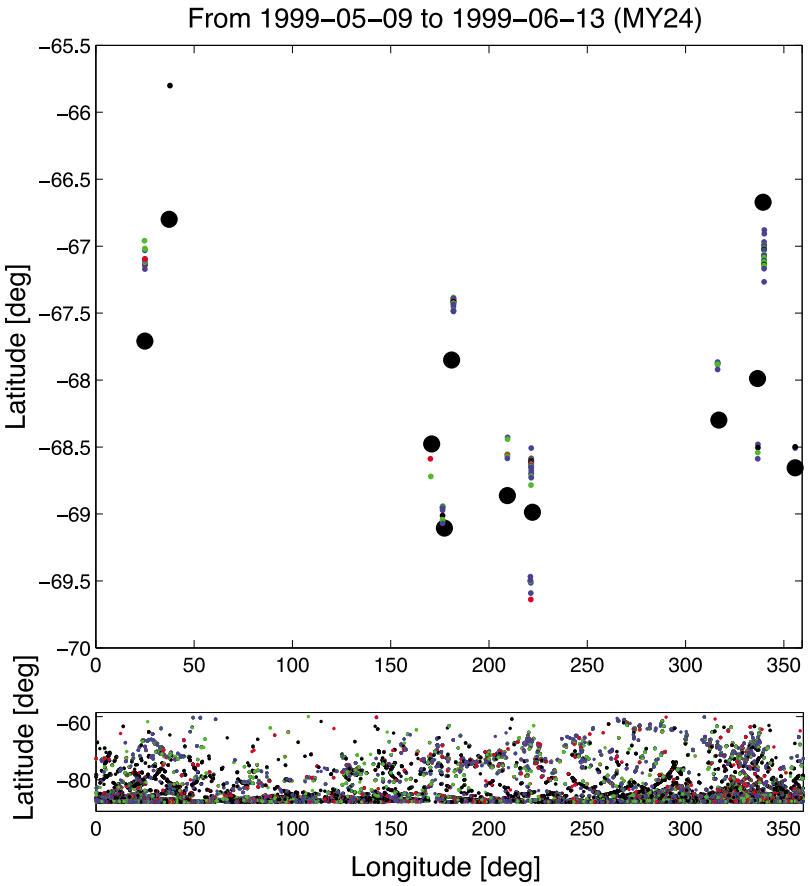

Figure 3. (top) Geographic Locations of MGS radio occultations and associated MOLA cloud detections from 1999 May 5 to 1999 June 13 in MY 24. Big black dots indicate the location of radio occultations, while small dots indicate the locations of corresponding MOLA cloud detections. Note that the range of latitude is significantly smaller than the range of longitude in this panel. (bottom) Locations of all MOLA non-ground returns during the same period. For both panels the colors indicate the MOLA filter channels: black is channel 1, red is channel 2, green is channel 3 and blue is channel 4.

words, a cloud detected by Channel 1 should have an opacity of $k \sim 0.3$ m^{-1}. Similarly, the Channel 2, 3, and 4 clouds should have opacity of $k \sim 0.1$, 0.04 and 0.01 m^{-1}, respectively.

[38] In the following, we relate the cloud opacities inferred from the MOLA echoes to the mass of CO_2 condensate particles per unit volume. As the MOLA return signal is reflected by the uppermost part of the CO_2 clouds, the mass estimates correspond to the uppermost part of the clouds. However, we do not intend to model the cloud microphysics on Mars; rather, we intend to provide a benchmark quantity, as measured by MOLA, for the content of CO_2 condensates in Mars' atmosphere when the temperature profile indicates saturation.

[39] For simplicity, we assume that the CO_2 condensate particles are spheres that follow a lognormal size distribution. The size distribution is controlled by various physical processes including nucleation, condensational growth, aggregation and precipitation, and depends on the atmospheric convection. We parameterize the particle size distribution by a lognormal distribution, which is regularly used in atmospheric applications [e.g., *Seinfeld and Pandis*, 2006]. The lognormal distribution employs two parameters: r is the average radius, and σ_g is the *geometric standard deviation* defined as the ratio of radius below which 84.1% of the particles lie to the median radius. This approximation simplifies the problem by describing the particle sizes with only two free parameters.

[40] The cloud opacity can be related to the mass of condensate particles via the particle size distribution. The opacity is related to the cross section of the particles as $k = n\sigma$, where n is the number density of the particles and σ is the cross section. The cross section of an individual condensate particle can be expressed as $\sigma = F\pi r^2$ where F is the extinction factor that can be calculated from the Mie theory of scattering. The mass of CO_2 condensate particles per unit volume (m) can then be related to the opacity as

$$m = k\frac{4r\rho}{3F}G_1, \tag{2}$$

where ρ is the mass density of individual CO_2 ice particle which we assume to be 1.5 g cm^{-3}, and G_1 is a geometric factor describing the size distribution of condensate particles. According to Mie theory, the extinction factor F depends on the refractive index of the material and size of particles. The refractive index of CO_2 ice at the MOLA 1.064 μm wavelength is $1.404 + 2.13 \times 10^{-6}i$ [*Warren*, 1996]. When

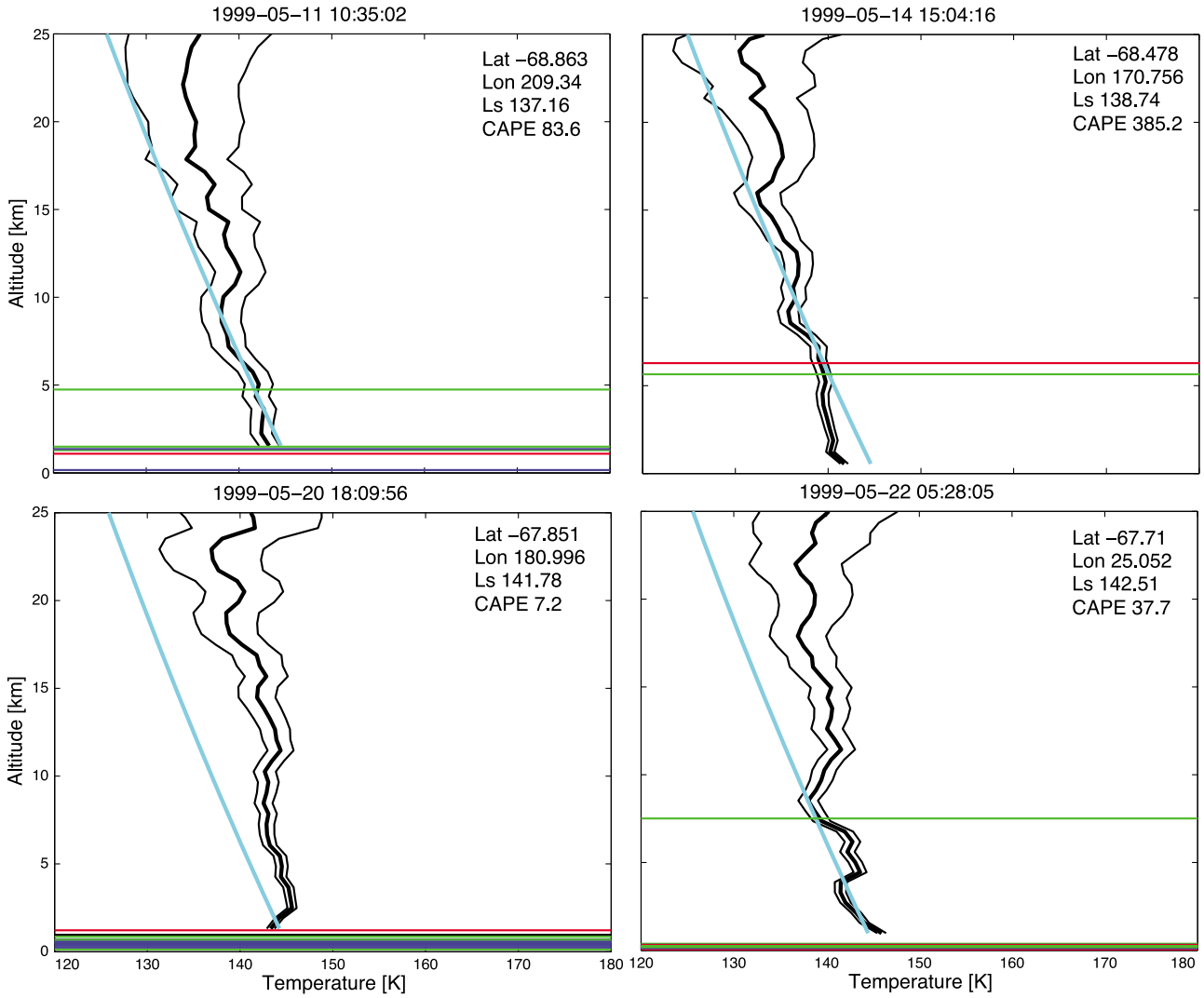

Figure 4. Temperature profiles measured by MGS radio science and associated MOLA cloud detections. The thick black curve shows the temperature profile, and the thin black curves show the uncertainties of temperature measurements. The title indicates the occultation time, defined as the time at Mars when the geometrical raypath grazed the limb. The text box tabulates the latitude, longitude and solar longitude of the occultation point, as well as the convective available potential energy (CAPE) in unit of J kg^{-1} as defined in *Colaprete et al.* [2003]. The cyan curve shows the condensation temperature of CO_2. The altitude is with respect to the local planetary radius produced by MOLA. The associated MOLA cloud detection events are shown by horizontal lines at corresponding altitudes. The color of these lines indicate the filter channel that triggered the cloud detection: black is channel 1, red is channel 2, green is channel 3 and blue is channel 4.

the particle radius is significantly larger than the wavelength, according to Mie theory, $F \sim 2$ and the mass of CO_2 condensate particles per unit volume indicated by a certain MOLA channel is proportional to the radius of individual particle. Also in this case, for the lognormal distribution, the geometric factor is

$$G_1 = \exp\left(\frac{5}{2}\ln^2\sigma_g\right). \quad (3)$$

The derivation of equations (2)–(3) are provided in Appendix B. We expect G_1 to be the order of unity. For example, $\sigma_g = 1.5$ represents a fairly wide size distribution, for which $G_1 = 1.5$. In the following, we assume G_1 to be unity unless otherwise specified. We address the degeneracy between r and σ_g in § 4.

[41] If the average radius of a CO_2 particle is 100 microns, the masses of the CO_2 condensates per unit volume for channel 1, 2, 3, and 4 clouds are 3.3×10^{-5}, 1.1×10^{-5}, 3.7×10^{-6} and 1.2×10^{-6} g cm^{-3}, respectively. We calculate the mass of CO_2 condensate particles per unit volume for various particle sizes using equation (2), and present the results in Figure 5. We verify in Figure 5 that when $r > 10\lambda$, the extinction factor F is constant and the mass is proportional to the particle radius. When $r < 10\lambda$, as predicted by

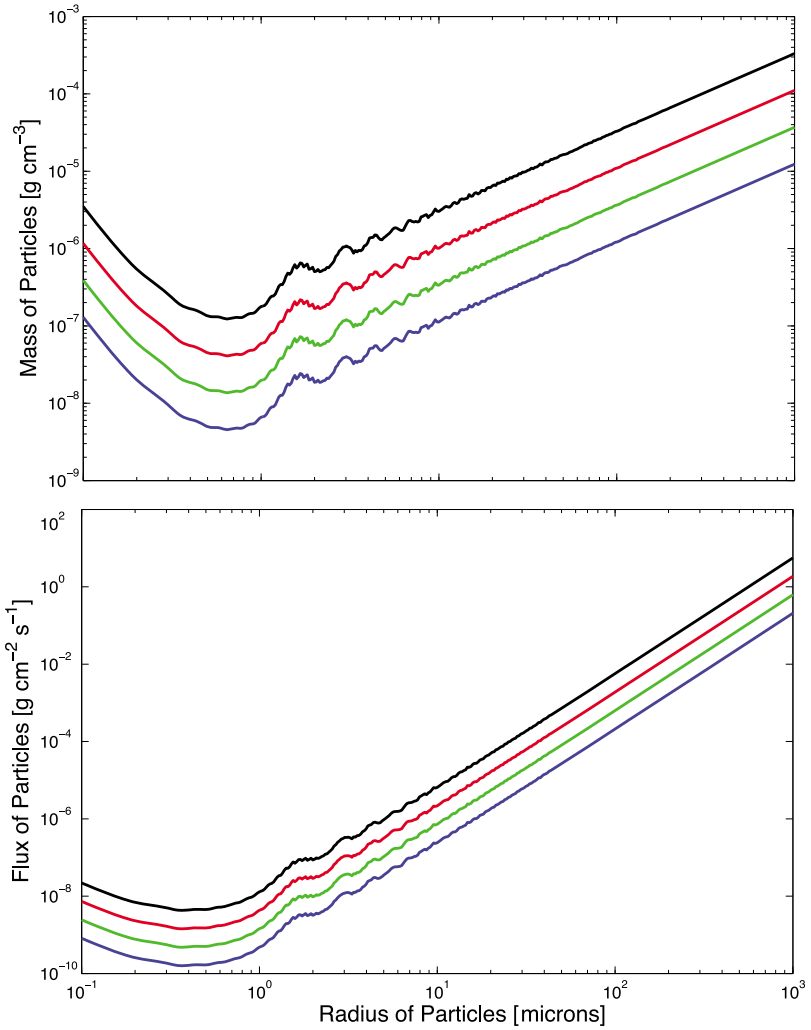

Figure 5. (top) The mass of CO_2 condensate particles per unit volume of clouds detected by MOLA filter channels with the geometric factor assumed to be unity. The black, red, green and blue lines correspond to MOLA channels 1, 2, 3, and 4, respectively. When the particle radius is significantly larger than the wavelength of MOLA ranging ($\sim 1\mu$m), the extinction factor F is constant and the mass is proportional to the radius; otherwise, the apparent features in the panel are predicted by Mie theory. (bottom) The steady state falling flux of CO_2 condensate particles of clouds detected by MOLA filter channels with the geometric factor assumed to be unity. The black, red, green and blue lines correspond to MOLA channels 1, 2, 3, and 4, respectively. The flux is computed with an ambient temperature of 150 k and pressure of 7 mbar.

Mie theory, F is variable and the complicated relationship between m and r is shown in Figure 5.

[42] We use the MOLA data to investigate how the mass of CO_2 condensate particles per unit volume depends on season. For each MOLA cloud return, we determine the cloud opacity according to the impulse response of the filter channel. For the northern and the southern hemispheres, MOLA cloud returns within the seasonal polar cap boundaries are selected and grouped into L_S bins of 5°. The average opacity of CO_2 clouds are shown in Figure 6. Using equation (2) we determine the average mass of CO_2 condensate particles per unit volume from the average opacity, also shown in Figure 6.

[43] The particle radius is the controlling factor of the mass of CO_2 condensate particles per unit volume. The mass scales linearly with the particle size. Although the mass estimate also depends on the MOLA filter channels (Figure 5), MOLA receives a large number of cloud returns, so that on average, the mass does not strongly depend on the season, except for a sudden increase of cloud opacity (and mass) at $L_S \sim 100°$. The average opacity indicated by all of the MOLA cloud returns is about 0.0005 cm^{-1}; the cloud opacity can be one order of magnitude higher during the middle winter of the southern hemisphere (Figure 6). The increase of the mean cloud opacity is due to a large number of Channel 1 cloud returns. The large population of MOLA channel 1 clouds has also been reported by *Ivanov and Muhleman* [2001] and *Neumann et al.* [2003]. The formation mechanism of Channel 1 clouds is still unknown. Also, for those MOLA cloud returns that are associated with MGS RS temperature profiles, we do not find any significant correlation between the cloud opacity and the CAPE.

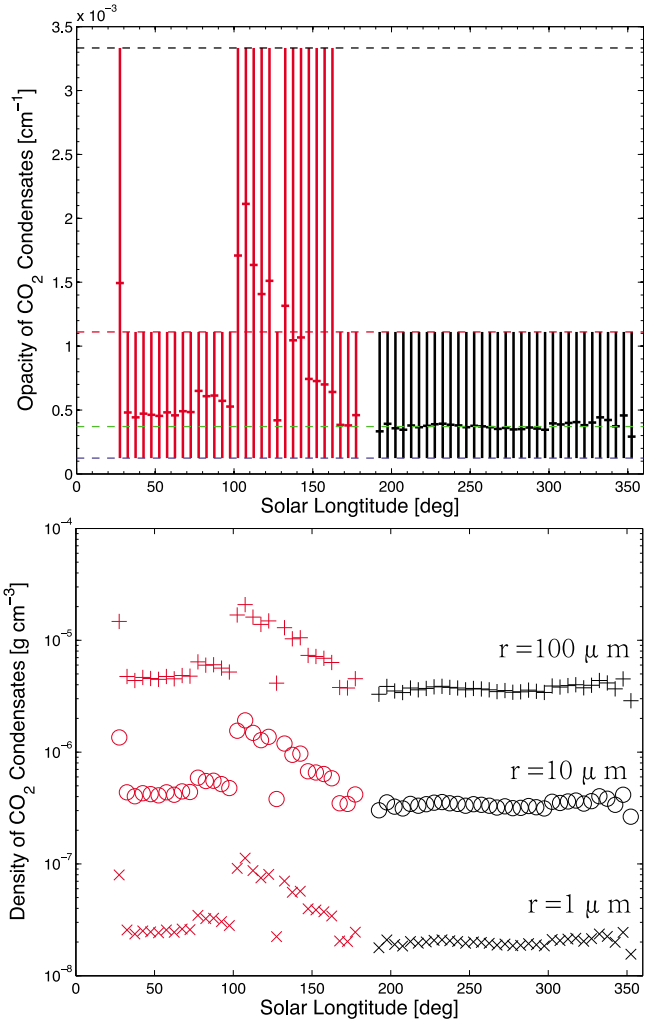

Figure 6. (top) Average opacity of CO_2 clouds and (bottom) mass of CO_2 condensate particles of different radii per unit volume measured by MOLA. The opacities and the masses are determined for each MOLA cloud return according to its filter channel, and the data within each L_S bin are averaged to give a mean value. Only MOLA returns that fall within the seasonal polar cap boundaries, defined in Figure 7, are used in the average. In Figure 6, top, the horizontal dashed lines indicate the opacities associated with 4 MOLA filter channels. The vertical error bars indicate the opacity ranges within which 80% of MOLA cloud returns in the corresponding L_S bin fall. In Figure 6, bottom, the red markers show the results for the southern seasonal polar cap in MY 25 and the black markers show the results for the northern seasonal polar cap in MY 24. The particle size is assumed to be 1 μm (crosses), 10 μm (circles), and 100 μm (plus signs), respectively. The geometric factor is assumed to be unity.

[44] Further, we compute the falling flux of CO_2 condensate particles. After condensation, the particles fall toward the surface at the settling velocity. The settling velocity can be reached when the gravitational force is balanced by the gas drag. The timescale for a particle to reach the settling velocity is very small. For example, aerosols with diameter in order of 1 μm can reach the settling velocity within 10^{-5} s in the terrestrial atmosphere [*Seinfeld and Pandis*, 2006]. Therefore, we assume the falling velocity to be the settling velocity. The settling velocity depends on the ambient atmosphere, and the formula can be derived from Stokes' law [*Seinfeld and Pandis*, 2006] as

$$v_F = \frac{2C_c}{9}\frac{r^2\rho g}{\mu}G_2, \tag{4}$$

where g is the gravitational acceleration, μ is the viscosity of the atmosphere, G_2 is another geometric factor related to the size distribution of particles, and C_c is the slip correction factor related to the mean free path (l) of the atmosphere:

$$C_c = 1 + \frac{l}{r}\left[1.257 + 0.4\exp\left(-\frac{1.1r}{l}\right)\right]. \tag{5}$$

The mean free path depends on the temperature and the pressure. At temperature of 150 K and pressure of 7 mbar, the mean free path of Mars' atmosphere is 2.2 μm. If the particle radius is significantly larger than the mean free path, $C_c \sim 1$, and then the settling velocity is proportional to the square of the particle radius. In cases of $C_c \sim 1$, for the lognormal size distribution, the geometric factor G_2 is

$$G_2 = \exp\left(2\ln^2\sigma_g\right). \tag{6}$$

We also expect G_2 to be the order of unity. For example, in the case of $\sigma_g = 1.5$, $G_2 = 1.4$. In the following, we assume G_2 to be unity unless otherwise specified. Stokes' law is valid when the Reynolds number Re $\ll$ 1. We verify that for an ambient temperature of 150 K and pressure of 700 Pa, Re < 0.1 for particles with a radius smaller than 44 μm. For larger particles, the settling velocity is smaller than the value estimated by equation (4) due to turbulence in the air. The settling flux of CO_2 condensate particles indicated by MOLA echoes is

$$\mathcal{F}_{\text{settle}} = mv_F. \tag{7}$$

The relationship between the settling flux and the average particle size is shown in Figure 5. Again we see that MOLA Channel 1 indicates the highest flux. When $r > 10$ μm, the settling flux depends on the particle radius as $\mathcal{F}_{\text{settle}} \propto r^3$, which is shown in Figure 5.

[45] To summarize, we report 11 events in MY 24 during which the MGS RS temperature profiles indicate CO_2 condensation and MOLA detects reflective clouds. Thus we provide causal evidence that MOLA non-ground returns are associated with CO_2 condensation, which strongly indicates their nature being CO_2 clouds. Using MOLA filter channels' temporal response as the probe of cloud opacities, we find that, on average, the particle size is the controlling factor of the mass of CO_2 condensates and the seasonal dependence of cloud opacities is a secondary factor. As a result, the mass and the settling flux of condensate particles mostly depend on the particle radius.

3.2. Area and Vertical Ranges of Mars Atmospheric CO_2 Condensation

[46] Starting from MY 28, the MCS samples the temperature profiles of Mars' atmosphere continuously and provides a unique opportunity to study the area and the vertical range

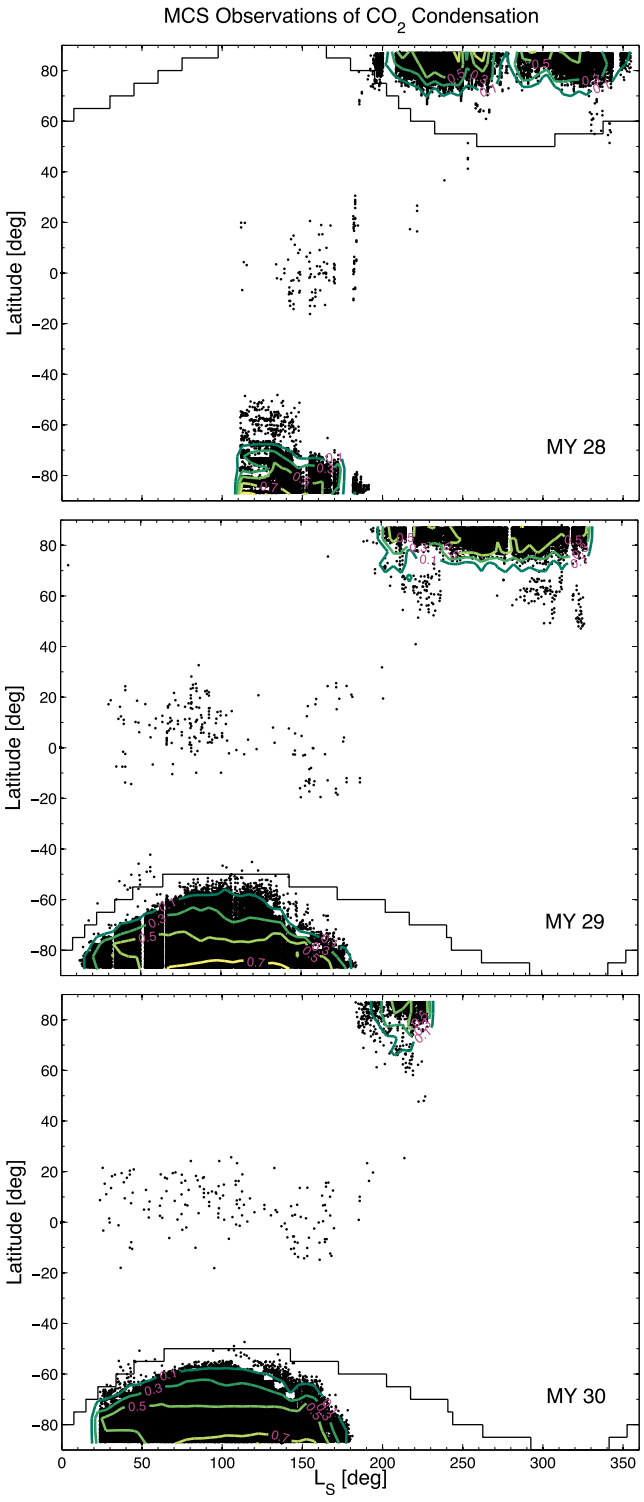

Figure 7. MCS observations of atmospheric CO_2 condensation. Temperature profiles that contain the CO_2 condensation layer are shown as black dots. Latitudes correspond to the areocentric (north) latitude of the occultation point, and L_S is measured positive with increasing time following the vernal equinox. The black curves show the seasonal polar cap model derived from TES bolometer observations [*Kieffer et al.*, 2000; *Kieffer and Titus*, 2001]. The contours in color show the occurrence rate of atmospheric condensation, which is decreasing from high latitude to low latitude.

of atmospheric CO_2 condensation. We focus on the seasonal and latitudinal behaviors of the CO_2 condensation.

3.2.1. Seasonal CO_2 Condensation Area

[47] Seasonal atmospheric condensation areas are clearly defined by the distribution of MCS temperature profiles that indicate CO_2 condensation. Latitudes and solar longitudes of MCS temperature profiles that contain a CO_2 condensation layer are shown in Figure 7. We note that the uncertainty of temperature retrieval of the MCS experiment increases with altitude and may become very large at low pressure (high altitude). Consequently, we exclude pressure levels whose temperature uncertainty is larger than 5 K from the comparison. As shown in Table 3 and in Figure 7, MCS provides consistent coverage over the entire polar area of the northern hemisphere in the winter of MY 28 and the whole polar area of the southern hemisphere in the winter of MY 29. We therefore use the MCS data to generate a template of seasonal boundaries of atmospheric condensation on Mars based on these two years, tabulated in Table 4. The template can be applied for general purposes, but we caution that the northern polar region in MY 28 may be affected by a planet-encircling dust storm during $L_s \sim 270°$–$305°$ observed by the Compact Reconnaissance Imaging Spectrometer onboard the MRO [*Smith et al.*, 2009a]. Heavy aerosol loading (dust, water ice, CO_2 ice, etc.) in the atmosphere may impede the temperature profile retrieval from MCS radiance measurements [*Kleinböhl et al.*, 2009], which leads to a significant reduction in the number of retrieved temperature profiles for Lat $\sim 60°$–$80°$ during the northern hemisphere winter.

[48] Not all temperature profiles within the seasonal boundaries of atmospheric condensation are saturated. First, we confirm with the MCS database that the atmospheric condensation on the dayside is negligible. Second, among those temperature profiles on the nightside, only a portion contain the condensation layer. We define the occurrence rate of atmospheric condensation as the ratio between the number of nightside temperature profiles that contain the condensation layer and the total number of nightside temperature profiles for a certain location and season. The occurrence rates are shown as over-plotted contours on Figure 7, in which we use L_S bin of 5° and latitude bin of 5°, so that in each bin the total number of temperature profile measurements are typically more than 500, which ensure the ratio statistically tracks the occurrence rate of atmospheric condensation. For the northern hemisphere Lat $\sim 60°$–$80°$ during the dust-storm season, the total number of temperature profiles in each bin may be reduced to 50, which still allows meaningful statistics. We find that the occurrence rate decreases from >0.5 at Lat > 85° to < 0.1 at the seasonal boundaries of atmospheric condensation. Fine seasonal dependence of the atmospheric condensation areas are illustrated in Figure 8, in which we use a box of 2-degree L_S and 5-degree Lat.

[49] The atmospheric condensation area determined from the MCS temperature profiles follows trends similar to the seasonal polar cap. Despite the minor data gaps during the northern hemisphere winter (see Figure 7) and a number of outliers, the analysis shows how the condensation area continually expands from autumn to winter and shrinks from winter to spring. As seen in Table 4, the atmospheric condensation area in the southern hemisphere reaches the most equator-ward latitude (~53°) at $L_S \sim 105°$ to 110°.

Table 4. Seasonal Boundaries of Mars Atmospheric CO_2 Condensation Derived from MCS Temperature Profiles[a]

North			South		
L_S(°)	Lat(°)	σ_{Lat}(°)	L_S(°)	Lat(°)	σ_{Lat}(°)
185–190	90.00	0	5–10	90.00	0
190–195	75.51	1.94	10–15	83.31	1.27
195–200	74.07	1.22	15–20	78.62	2.96
200–205	81.85	0.54	20–25	76.10	3.89
205–210	78.17	1.35	25–30	74.51	1.16
210–215	74.53	1.21	30–35	71.22	2.97
215–220	74.52	0.53	35–40	67.94	5.10
220–225	71.84	0.90	40–45	66.37	5.76
225–230	68.74	1.34	45–50	62.20	7.41
230–235	73.28	0.87	50–55	64.20	3.90
235–240	71.54	0.75	55–60	59.66	6.74
240–245	71.80	0.62	60–65	60.99	2.23
245–250	69.71	0.98	65–70	59.38	1.80
250–255	71.08	7.45	70–75	58.21	2.20
255–260	69.22	3.62	75–80	56.07	1.10
260–265	68.02	5.52	80–85	55.47	1.35
265–270	68.66	3.59	85–90	55.65	1.51
270–275	74.85	1.89	90–95	54.68	1.28
275–280	78.88	2.59	95–100	54.44	0.77
280–285	78.46	2.12	100–105	53.27	2.59
285–290	76.33	1.89	105–110	53.26	2.21
290–295	76.48	1.02	110–115	54.19	2.33
295–300	77.91	1.02	115–120	54.60	2.43
300–305	81.00	0.50	120–125	54.25	1.69
305–310	76.85	0.49	125–130	55.27	1.75
310–315	75.21	1.41	130–135	56.19	2.09
315–320	73.79	1.17	135–140	60.44	1.59
320–325	74.49	0.65	140–145	64.06	4.72
325–330	71.59	3.33	145–150	64.38	3.65
330–335	60.55	3.66	150–155	68.48	2.78
335–340	66.37	6.88	155–160	72.32	1.78
340–345	59.93	7.88	160–165	73.62	1.90
345–350	80.90	1.09	165–170	72.97	2.82
350–355	79.34	1.91	170–175	75.37	2.25
355–360	90.00	0	175–180	78.50	1.39
			180–185	85.39	1.29
			185–190	90.00	0

[a]Latitudes of saturated temperature profiles measured by the MCS during MY 28 (North) and MY 29 (South) are used to determine the seasonal boundaries, whose values and uncertainties are defined as the average and the standard deviation of the 10 most equator-ward latitudes in each L_S bin of 5°. For those L_S bins that have less than 10 qualified temperature profiles, the boundary is set to 90°. The cutoff number 10 is arbitrarily chosen, and we have verified that changing this cutoff number from 5 to 20 yields nearly the same results.

Otherwise, the atmospheric condensation area in the northern hemisphere remains within about latitude ~70° from $L_S \sim$ 190° to 330°, and then extends to about latitude ~60° from $L_S \sim$ 330° to 345°. In comparison, the seasonal polar cap size model derived from the variation of surface albedo and brightness temperatures measured by TES solar and thermal bolometer observations extends to Lat ~ 50° in the middle of winter in both hemispheres [*Kieffer et al.*, 2000; *Kieffer and Titus*, 2001; *Smith et al.*, 2009b].

[50] The seasonal polar cap derived from TES bolometer observations is larger than the area of atmospheric CO_2 condensation, indicating the contribution of surface direct deposition. As seen in Figure 7, in autumn, the expansion of seasonal polar caps observed by TES correlate with condensation of CO_2 very well, which provides evidence that condensation of atmospheric CO_2 contributes significantly to the formation of the seasonal polar caps. In spring, the seasonal polar cap derived from TES bolometer observations has an extended "tail", when condensation of CO_2 stops. This period corresponds to sublimation of CO_2 and water ice and the shrinking of seasonal polar caps, which are not considered in this work. Particularly for the northern hemisphere, the area of CO_2 condensation is much smaller than the seasonal polar cap derived from TES (see Figure 7). The seasonal polar cap beyond the atmospheric condensation area is mostly due to surface direct deposition of CO_2 mixed with minor amounts of water ice [*Kieffer and Titus*, 2001; *Wagstaff et al.*, 2008].

[51] Atmospheric condensation in the northern hemisphere has more intense seasonal variation than in the southern hemisphere. The occurrence rates of atmospheric condensation are highly variable at the same latitudes in the northern hemisphere, which indicates that the condensation in the northern hemisphere may be composed of multiple independent weather events, i.e., snow storms (see Figure 8). The temporal changes of atmospheric condensation are more evident near the lower-latitude boundary of the polar region. In comparison, atmospheric condensation in the southern hemisphere is relatively stable throughout the whole winter. The seasonal variation of atmospheric condensation in the northern polar region may be related to the development of baroclinic waves. Numerical simulations have suggested strong transient baroclinic wave activity in Mars' northern midlatitude region during the northern autumn, winter and spring seasons [*Barnes et al.*, 1993]. The baroclinic waves have periods of 2 to 6 sols and create eddies that transfer heat from low latitudes to high latitudes [*Barnes et al.*, 1993; *Kuroda et al.*, 2007]. The baroclinic activity in the northern hemisphere has also been observed from the MGS RS temperature profile measurements [*Hinson*, 2006]. The MCS data shows intense weather in the northern polar region during the northern hemisphere autumn and winter.

[52] Dust storms may have a profound effect on atmospheric CO_2 condensation on Mars. We notice that at the same time as the planet-encircling dust storm, the size of seasonal polar cap decreases by ~10° and lasts for ~20° L_S after the dust storm. We caution that few MCS temperature profiles can be retrieved during this period for the northern polar region. However, as shown in Figure 8, the occurrence rate of atmospheric condensation is also very low during the dust storm. Therefore, it is unlikely that observational bias can be solely responsible for the apparent deficit of the atmospheric condensation during the dust storm. A dusty atmosphere absorbs more solar radiation and therefore has higher temperature so the condensation of CO_2 may not occur. Although there is no insolation during the polar night when the atmospheric condensation occurs, atmospheric circulation can transport the heat to the north polar region and suppress the condensation [e.g., *Forget et al.*, 1998].

[53] Seasonal and latitudinal trends of atmospheric CO_2 condensation are consistent with cold spot activity. Defined as unrealistically low brightness temperatures, cold spots have been interpreted as fresh CO_2 snow on Mars' surface [e.g., *Forget et al.*, 1995; *Titus et al.*, 2001; *Cornwall and Titus*, 2009, 2010]. Similar to the atmospheric condensation, the formation of cold spots in the northern hemisphere is found to be more patchy and more latitudinally confined

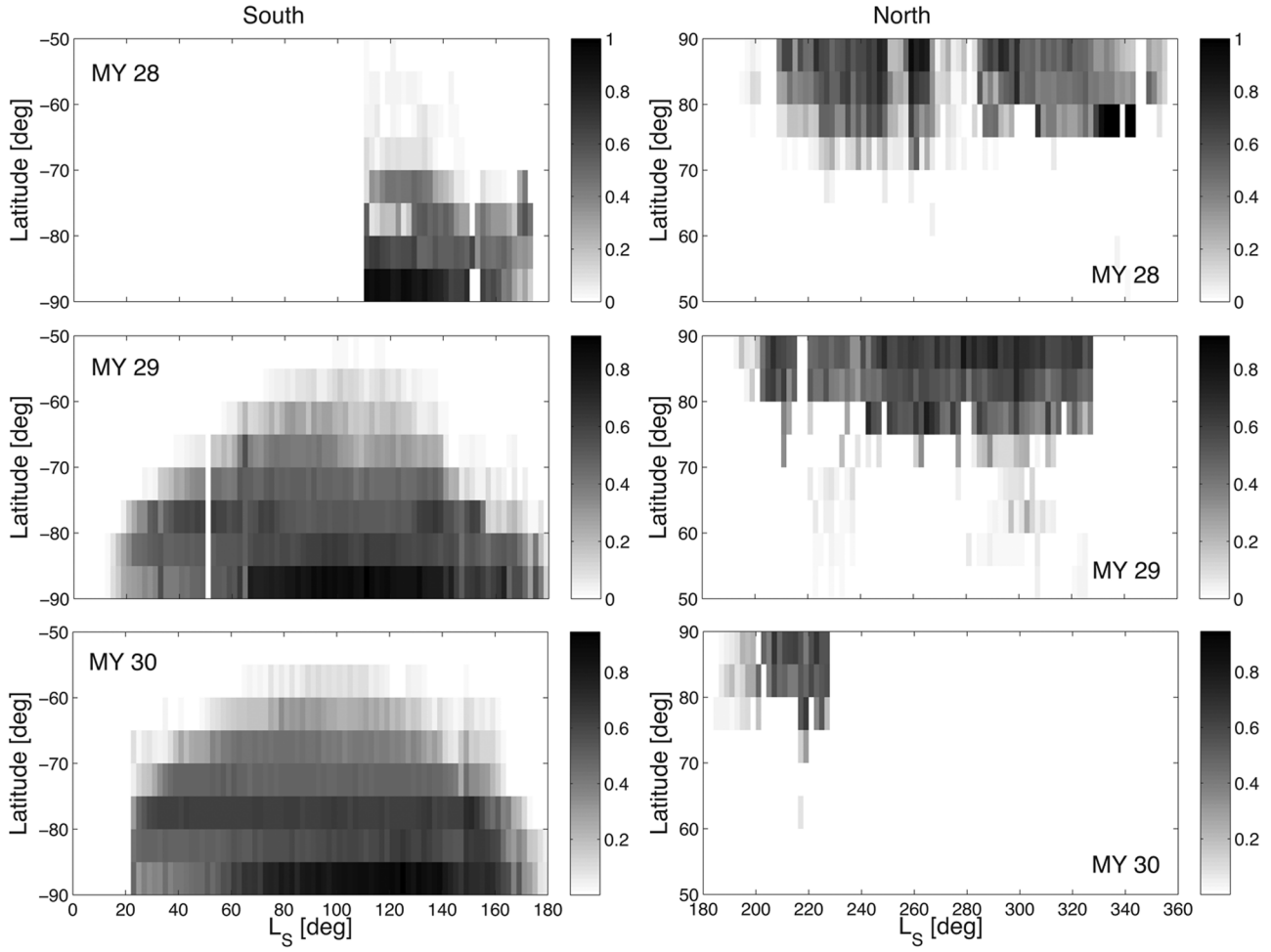

Figure 8. Occurrence rates of atmospheric condensation on Mars as measured by the MCS. The occurrence rates are color-coded, defined as the ratio between the number of nightside temperature profiles that contain the condensation layer and the total number of nightside temperature profiles in each box of 5-degree Lat and 2-degree L_S. Note that the occurrence rate generally decreases from high latitudes to low latitudes, with apparent fine structure peculiarities. Atmospheric condensation in the northern hemisphere has more intense seasonal variations than in the southern hemisphere. We note that there are less than 10 MCS profiles per each bin in MY 28 for $L_S \sim 202°$–$208°$, $L_S \sim 280°$–$282°$ and $L_S \sim 306°$–$360°$ and Lat $\sim 60°$–$75°$N, in which we do not assess the occurrence rate.

than in the southern hemisphere [*Cornwall and Titus*, 2009, 2010]. The north–south difference in the cold spot activity may be due to the fact that condensation due to topographic lifting is more common in the northern hemisphere [*Forget et al.*, 1998; *Colaprete and Toon*, 2002; *Tobie et al.*, 2003; *Cornwall and Titus*, 2010]. Also, evidence shows that dust storms may suppress the formation of cold spots in the northern hemisphere [*Cornwall and Titus*, 2009], which is consistent with our results.

[54] Two additional observations are worth noting. First, in Figure 7 it is surprising that some temperature profiles above the equatorial region (Lat < 40°) also contain a CO_2 condensation layer. We examined these temperature profiles individually, and found that the condensation layers of these profiles correspond to pressures of 0.1 to 1 Pa. The condensation layers above the equatorial region are at a higher altitude than those above the polar region shown in Figure 1. *Montmessin et al.* [2006] found high-altitude CO_2 clouds in the southern winter subtropical latitudes of Mars by observing stellar occultations. The clouds are located where simultaneous temperature measurements indicate saturation of CO_2. We find similar CO_2 high-altitude condensation layers above the equatorial region of Mars during the southern winter based on the MCS temperature-pressure profiles, as shown in Figure 7. This phenomenon of equatorial high-altitude supersaturation has also been reproduced in a Mars General Circulation Model (MGCM) [*Colaprete et al.*, 2008], and interpreted as a result of mesoscale gravity waves in Mars' atmosphere [*Spiga et al.*, 2012]. The equatorial high-altitude supersaturation occurs mostly during the southern fall and winter, which differs in seasonal behavior from the MGCM. Second, we do not consider the zonal behavior of atmospheric condensation in this study. It has been shown that the cold spots tend to concentrate in a certain

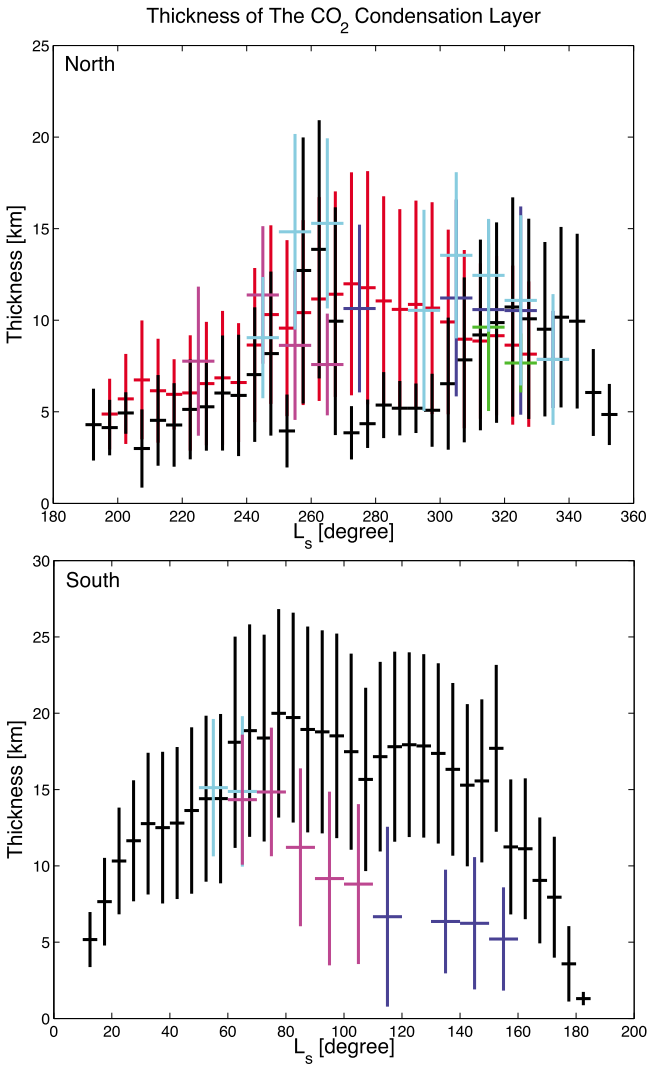

Figure 9. Thickness of the CO_2 condensation layer above the Mars poles from MY 24 to MY 29. Temperature profiles above the seasonal polar caps measured by the MRO MCS and the MGS RS experiment are used to determine the thickness of the CO_2 condensation layer. Individual values of the thickness are grouped into L_S bins of 5° (for MCS) or 10° (for MGS RS). For each bin, the mean value and statistical standard deviation are shown. To ensure the statistical significance, we only show the values of the L_S bins in which there are more than 10 measurements that indicate CO_2 saturation. (top) North: blue = MY24 (MGS RS), green = MY25 (MGS RS), magenta = MY26 (MGS RS), cyan = MY27 (MGS RS), black = MY28 (MCS), and red = MY29 (MCS); (bottom) South: blue = MY24 (MGS RS), cyan = MY27 (MGS RS), magenta = MY28 (MGS RS), and black = MY29 (MCS). Suppression of the CO_2 condensation layer in the northern hemisphere in mid-winter in MY 28 may be related to a planet-encircling dust storm that occurred during $L_S \sim 270°$–$305°$.

longitude range (30°E–90°W) outside the polar night in the southern hemisphere [*Cornwall and Titus*, 2010], consistent with the zonal distribution of the CAPE found by MGCM [*Colaprete et al.*, 2005, 2008].

[55] Finally we compute the total area of the CO_2 condensation on Mars. We define the integrated condensation area time (ICAT) as

$$\mathrm{ICAT} = \int_{\mathrm{winter}} \int_{\mathrm{pole}} P(\mathrm{Lat}, t) R_N(\mathrm{Lat}, t) A(\mathrm{Lat})\, d\mathrm{Lat}\ dt, \qquad (8)$$

where P is the occurrence rate of atmospheric condensation, R_N is the fraction of nighttime as a function of season and latitude, A is the area of each latitude bin, and t is the time. Using the data presented in Figure 8 together with the Keplerian motion of Mars, we determine for the north winter of MY 28, ICAT = $2.12 \pm 0.57 \times 10^{19}$ m^2 s; for the south winter of MY 29, ICAT = $7.42 \pm 1.14 \times 10^{19}$ m^2 s; and for the south winter of MY 30, ICAT = $8.93 \pm 0.94 \times 10^{19}$ m^2 s. The uncertainties correspond to a combination of the temperature standard deviation of each MCS profile and the statistical sampling errors inversely proportional to the square root of the number of measurements in each bin. In essence, the ICAT corresponds to the weighted integration of the shaded areas in Figure 8. The horizontal axis of Figure 8 is L_S, so we have converted dL_S to dt based on the Keplerian motion of Mars. We find that the ICAT of the southern hemisphere is more than three times larger than that of the northern hemisphere, due to a larger condensation area and a longer period in winter. The value of the ICAT will be useful to estimate the total mass of CO_2 precipitation per winter.

3.2.2. Thickness of the Condensation Layer

[56] Based on the temperature profiles measured by the MRO climate sounder (MCS) and the MGS RS experiment, we determine the thickness of the CO_2 condensation layer in Mars' atmosphere, and see how the thickness varies with season. Thanks to a long period of monitoring by MGS and MRO, we may also compare the thickness of the condensation layer from Mars year to Mars year and study the interannual variability.

[57] Figure 9 shows thickness of the CO_2 condensation layer above the Mars' seasonal polar caps from MY 24 to MY 29. For this analysis, we process the data from different Mars years independently, and present the results with different colors. Condensation layer thickness is determined from each of the temperature profiles measured by MCS or MGS RS. Individual thickness values are grouped into L_S bins of 5° (for MCS) or 10° (for MGS RS). Only the temperature profiles measured within the seasonal polar caps are taken into account. For the MCS data, the seasonal polar cap boundary is determined the same way as in section 3.2.1, and is also independent from year to year. For the MGS RS data, the seasonal polar cap boundaries are assumed to be at the latitude of 50° for both the northern and the southern hemisphere. For each L_S bin, if the number of valid measurements in that period exceeds 10, we compute the mean and the standard deviation of the thickness, and show the results in Figure 9.

[58] The MCS provides more temperature profile measurements than MGS RS, which allows us to use smaller L_S bins. The data from the MCS temperature measurements yield the thickness results for the entire northern hemisphere winter of MY 28, the entire southern hemisphere winter of MY 29, and a significant part of northern hemisphere winter

(up to $L_S \sim 330°$) of MY 29. As seen in Figure 7, MCS densely samples all latitudes within the seasonal polar caps at different seasons, which makes the average thickness presented in Figure 9 independent of the latitude. MGS RS has fewer measurements that seasonally cover the polar caps (see Table 2). In addition, there is a strong correlation between the latitude and the L_S for the MGS RS measurements. As a result, for those average values derived from the MGS RS data, although grouped in L_S bins, it is unclear whether the apparent dependency is on the season or on the latitude. In summary, the MCS instrument provides a data set with dense global coverage to be used to measure the thickness of the CO_2 condensation layer in Mars' atmosphere, shown in black and red colors in Figure 9; whereas one should be more cautious when interpreting the average thickness synthesized from the MGS RS data, also shown in Figure 9 but with other colors.

[59] As shown in Figure 9, condensation of CO_2 in Mars' atmosphere is a seasonally repetitive process. Within the uncertainties, the thicknesses of the condensation layer in different Mars years agree with each other. For the northern hemisphere, condensation of CO_2 starts at $L_S \sim 190°$, and then the layer gradually expands to about 10–15 km as L_S increases to $\sim$260°. This trend is demonstrated by both the MCS data and the MGS RS data. As the planet moves into northern spring, the thickness of the condensation layer gradually decreases, also shown by data of different Mars years. Also, for the southern hemisphere, the thickness of condensation layer expands at the beginning of winter and shrinks at the end of winter. Again, the comparison among the measurements of MGS RS in MY 27 and the measurements of MCS in MY 28 and 29 indicate the repeatability of CO_2 condensation during winters. The MGS RS and the MCS measurements give generally consistent descriptions on the seasonal variation of CO_2 condensation in Mars' atmosphere.

[60] Despite the periodicity, there is also some interesting interannual variability. Above the northern polar cap, suppression of the condensation layer in the middle of winter from $L_S \sim 270°$ to $\sim$300° is observed in MY 28 (see black color in Figure 9, top). As a comparison, in MY 29, the condensation layer remains at its maximum thickness during the middle of winter (see red color in Figure 9, top). The suppression also does not take place in MY 24, suggested by the MGS RS measurements (see blue color in Figure 9, top). Again, the suppression of the condensation layer during the middle of winter in MY 28 may be due to the major dust storm. We see that not only horizontal extent but also vertical extent of atmospheric condensation can be affected by dust storms.

[61] The comparison between Figures 9 (top) and 9 (bottom) indicates that condensation of CO_2 occurs over greater vertical extent of Mars' atmosphere in the southern hemisphere than in the northern hemisphere. The thickness-L_S plot (Figure 9) shows a "plateau" shape for both the northern hemisphere and the southern hemisphere. For the north, the plateau indicates a thickness of about 10–15 km from $L_S \sim 250°$ to $\sim$340°; and for the south, the plateau indicates a thickness of about 20 km from $L_S \sim 70°$ to $\sim$160°. The CO_2 condensation layer above the southern polar cap is 5–10 km thicker than that above the northern polar cap.

3.3. Estimation of Condensation Masses

[62] We estimate the total mass that condenses and falls onto the seasonal polar cap during a Martian winter from the MCS and MOLA data. The total precipitation mass can be computed from the following integration

$$\mathcal{M}_{\mathrm{pr}} = \int_{\mathrm{winter}} \int_{\mathrm{pole}} \mathcal{F}(t) P(\mathrm{Lat}, t) R_N(\mathrm{Lat}, t) A(\mathrm{Lat})\, d\mathrm{Lat}\; dt, \quad (9)$$

in which $\mathcal{F}$ is the precipitation flux in unit of kg m^{-2} s^{-1}, P is the occurrence rate of atmospheric condensation, R_N is the nighttime fraction, and A is the area of each latitude bin. Using the settling flux derived in section 3.1.3 as the probe of the precipitation flux ($\mathcal{F}$) and the ICAT derived in section 3.2.1 as the probe of the spatial extent of precipitation, we can evaluate equation (9).

[63] Substantial simplifications have to be made in order to estimate the total condensation mass. We use in this estimate the settling flux defined by equation (7) and measured by MOLA as a proxy to the precipitation flux on Mars, i.e., assuming $\mathcal{F} = \mathcal{F}_{\mathrm{settle}}$. However, actual precipitation processes might be much more complex, which depends on small-scale atmospheric circulation. MOLA only probes the uppermost part (up to 81 m) of the clouds. The precipitation flux that leaves the clouds would depend on the dynamics inside the clouds, which is typically treated as stochastic processes in atmospheric modeling [e.g., *Rogers and Yau*, 1989]. In addition, the precipitating CO_2 may evaporate as it settles, if the near surface layer is not saturated (see Figure 1). Also, it has been suggested that some of the MOLA clouds are associated with topographic features [*Pettengill and Ford*, 2000; *Colaprete and Toon*, 2002; *Cornwall and Titus*, 2009, 2010]. Currently available atmospheric data do not yet encourage detailed analyses regarding the cloud microphysics and the dynamics of condensate particles.

[64] Despite the simplifications, equation (9) captures the main physics of atmospheric condensation and precipitation. First, the precipitation flux, a highly variable parameter, is found to have little dependence on the season (see Figure 6). The uncertainties assigned for cloud opacities, from which the precipitation flux is estimated, are fairly large (a factor of 3) and generally independent of season as well. Second, the fact that cloud formation and precipitation are local and discontinuous events is accounted for by multiplying by the occurrence rate of atmospheric condensation P, which is defined as the ratio between the number of saturated temperature profiles and the total number of retrieved nighttime profiles for each 2° L_S and 5° Lat bin. Finally, R_N accounts for the fact that atmospheric condensation almost exclusively happens during the nighttime. In all, equation (9) relates the atmospheric condensation and precipitation of CO_2 during a Mars polar winter to observables in an average sense, and is suitable for the first attempt to observationally estimate the atmospheric condensation mass on Mars.

[65] The only unknown parameter in the estimate of the total condensation mass is the average particle size, which relates the precipitation flux to the cloud opacity. As shown by equation (7) and Figure 5, the local precipitation flux depends on the average particle radius as $F \propto r^3$ if the particles are larger than a few μm in size. Consequently, the total

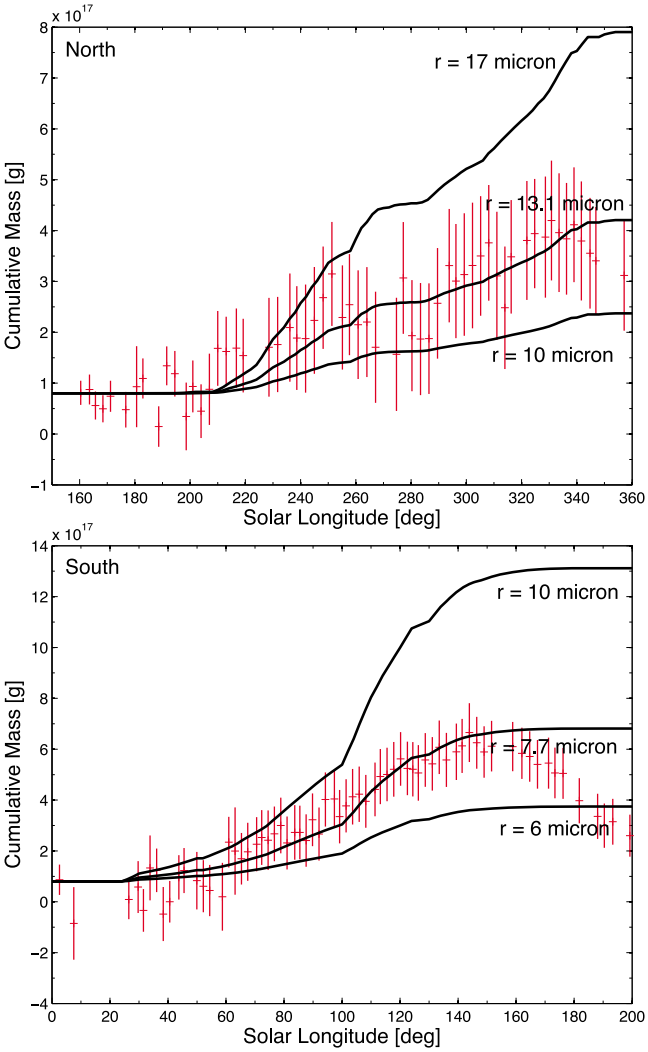

Figure 10. Estimated cumulative masses of the northern seasonal polar cap and the southern seasonal polar cap. The data points in red are the seasonal polar mass values retrieved from the variation of Mars' gravity field, in MY 24 for the northern hemisphere and MY 25 for the southern hemisphere [*Smith et al.*, 2009b], scaled by a factor of 0.1 to account for the contribution of surface direct deposition. The black curves in the middle are the best fitted estimates of cumulative masses of CO_2 condensation with the geometric factor assumed to be unity, and the other black curves show the effect of variation of particle sizes. The estimates use seasonal area of atmospheric CO_2 condensation measured by MCS and seasonal masses of condensate particles per unit volume measured by MOLA. The estimates of the total mass of CO_2 condensation are independent from the values retrieved from the gravity variation. For the best fitted estimates, the average particle radius is 13.1 μm for the northern hemisphere and 7.7 μm for the southern hemisphere.

condensation mass depends on the average particle radius as $\mathcal{M}_{pr} \propto r^3$. In addition, the geometric factors affect the precipitation flux and then the total mass, which we generally assume to be unity.

[66] We compare the total condensation mass to the seasonal polar cap masses. Both atmospheric precipitation and surface direct deposition contribute to the formation of Mars' seasonal polar caps. For convenience we define F_P as the ratio between the mass of atmospheric condensation and the mass of seasonal polar cap. It has been suggested from general circulation simulations that the atmospheric precipitation contributes about 10% of the mass in seasonal caps [*Colaprete et al.*, 2005, 2008], or $F_P \sim 0.1$. We note that F_P can vary up to 0.9 depending on the season and the geographic location [*Colaprete et al.*, 2005]; so on average, we assume that F_P has an uncertainty of a factor of 3. We can subsequently constrain the average particle size by fitting the atmospheric condensation mass to the seasonal polar cap mass scaled by F_P, i.e., $\mathcal{M}_{pr} \sim \mathcal{M}F_P$ where $\mathcal{M}$ is the seasonal polar cap mass independently inferred from the variation of Mars' gravitational field [*Smith et al.*, 2009b]. In practice, an arbitrary offset $\mathcal{M}_i$ needs to be added to the seasonal polar masses. We fit our estimate to the seasonal polar mass values measured by the gravity variation during MY 24 for the northern hemisphere and MY 25 for the southern hemisphere (the same Mars years as the MOLA data), and the best fitted models are presented in Figure 10.

[67] The amount of CO_2 condensation estimated based on the MCS temperature profiles and MOLA cloud returns follows the variation of seasonal polar mass. As seen in Figure 10, the masses estimated in this work are generally consistent with the seasonal dependence of the masses inferred from the gravity variation. In particular, the starting L_S and the ending L_S of atmospheric precipitation are consistent with the mass accumulation on Mars' north and south poles inferred from the gravity, implying a seasonal coherence between the atmospheric condensation and the surface direct deposition. In the best fitted model, the average particle radius is r = 13.1 μm for the northern hemisphere and r = 7.7 μm for the southern hemisphere. We confirm that the particle size is indeed large enough for the precipitation flux to scale with the particle size as $F \propto r^3$, which allows the particle size to be uniquely determined by comparing the total precipitation flux to the seasonal polar cap masses.

[68] We estimate the uncertainties of the total mass and the particle size as follows. For a certain average particle radius, the uncertainty of the total condensation mass is a factor of 3, which is propagated from the uncertainties in the occurrence rate of atmospheric condensation and the uncertainties in the cloud opacity. The uncertainty of atmospheric condensation represents the error due to limited sampling of Mars' atmosphere by the MCS; and the uncertainty range of cloud opacity covers 90% of cloud returns by MOLA. The uncertainties of the cloud opacity and therefore the precipitation flux contribute the most part of the uncertainty (see Figure 6). Furthermore, the uncertainty of our average particle radius estimates should include the uncertainty of F_P, which we have assumed to be a factor of 3. Also taking into account the scaling relationship $r \propto \mathcal{M}_{pr}^{1/3}$, we estimate the combined uncertainty of average particle radius to be a factor of 1.7. With uncertainties, the average CO_2 condensate particle radius is estimated to be 8–22 μm in the northern hemisphere and 4–13 μm in the southern hemisphere. We find that the estimated average particle radius above the northern seasonal

polar cap is marginally larger than that above the southern seasonal polar cap.

4. Discussion

4.1. Cloud Formation on Mars

[69] The nature and formation mechanism of MOLA reflective clouds remain largely uncertain. When the atmosphere becomes supersaturated, CO_2 molecules may condense if nucleating sites are available. In the Martian atmosphere, the most likely nucleating sites are dust grains and water ice grains. *Pettengill and Ford* [2000] suggest that MOLA clouds are associated with topographic features, suggesting them to be mountain wave clouds. *Colaprete and Toon* [2002] demonstrate that some of the MOLA echoes are consistent with orographic cloud formation (mountain waves) with detailed 1-D dynamical and cloud formation model. In this work, we provide observational evidence that MOLA clouds form from condensation of CO_2. We find that the supersaturation in the Martian atmosphere is limited and condensation of CO_2 effectively keeps the temperature profiles along the saturation curve of CO_2. Together with the association of the MOLA clouds and surface cold spots [*Ivanov and Muhleman*, 2001], these snap-shots of atmospheric condensation and precipitation on Mars are relatively complete.

[70] Of particular interest are the MOLA Channel 1 clouds. *Neumann et al.* [2003] suggest that Channel 1 hits come from either large reflective individual CO_2 particles of size 1 cm, or diffuse crystalline flakes. The microphysical study of *Colaprete et al.* [2003] indicates that it is difficult to generate CO_2 ice particles larger than 0.1 cm. Also, the settling velocity of a 1-cm particle is 5 m s^{-1} in a 7 mbar atmosphere and the particle should fall to the ground in about 10 min. *Colaprete et al.* [2003] then propose that the clouds detected by the MOLA Channel 1 should be small and concentrated CO_2 crystals, formed from convective uplift which could be initiated with orographic lifting. The Channel 1 clouds have the highest opacity which indicates the largest concentration of CO_2 condensate particles per unit volume (see Figure 5). These clouds are mostly detected during mid-winter in the southern hemisphere (see Figure 6).

[71] A clear distinction between north and south cloud formation is revealed by our analysis. The occurrence rate of atmospheric saturation in the northern hemisphere derived from the MCS data set shows that the saturation in the northern polar region generally only extends to latitudes of about 75°, with temporal variations that extend to lower latitudes (about 70°). Spectral analysis of the condensation occurrence rates as a function of L_S cannot find any significant modes with a period longer than 2° L_S. The current seasonal bin size is probably comparable or larger than the intrinsic period of the temporal variation, consistent with the periods of baroclinic waves [*Barnes et al.*, 1993]. Finer seasonal structures of atmospheric condensation cannot be resolved since the number of MCS profiles becomes too small for statistical study if L_S bin size is less than 2°. In the southern hemisphere, the atmospheric saturation is more stable and extends to much lower latitudes (about 60°) in the middle of winter than in the northern hemisphere (see Figure 8). Numerical simulations have suggested that the baroclinic wave activity is much weaker in the southern winter than in the northern winter, probably due to larger extent of the southern seasonal polar cap and high elevations in the southern hemisphere [*Barnes et al.*, 1993]. The detailed relationship between the baroclinic wave activity and the atmospheric condensation in Mars' polar regions has yet to be explored by general circulation theories.

4.2. Size of CO_2 Condensate Particles

[72] In this paper, we estimate the average radius of CO_2 condensate particles to be 8–23 μm in the northern hemisphere and 4–13 μm in the south. The particle radius is inferred by comparing the total mass of CO_2 condensation to the seasonal polar mass derived from the gravity variation, scaled by the factor F_P. We introduce the factor F_P to include the uncertainty of the contribution of atmospheric precipitation in the formation of seasonal polar caps. The nominal value of F_P is 0.1 and the uncertainty is a factor of 3 [*Pollack et al.*, 1990; *Colaprete et al.*, 2005]. In the estimate of the total mass of CO_2 condensation, the MCS temperature profiles indicate the spatial extent in which condensation of CO_2 occurs, and the MOLA cloud returns indicate the concentration of condensate particles in the atmosphere. We use the settling flux of the MOLA detected condensate particles as the proxy to the precipitation flux. The combination of information from these two instruments allows us to reduce the free parameters to be the average particle radius (r) and the geometric factor (σ_g) describing the size distribution. Based on atmospheric physics, our estimates of the total mass of CO_2 condensation are independent of the values retrieved from the gravity variation, and then we may use the gravity-inferred seasonal polar mass to constrain the average particle radius.

[73] It is worthwhile to summarize the sources of uncertainty in the estimate of particle radius. The uncertainties of the particle size estimate contain the uncertainties of condensation area and occurrence rate derived from the MCS data set, the uncertainties of cloud opacities measured by MOLA echoes, and the uncertainties of F_P. All these uncertainties are combined as independent errors and propagated into the final results. Notably, the condensation mass depends on the particle size as $\mathcal{M}_{\rm pr} \propto r^3$, which allows the particle size to be reasonably determined despite large uncertainties in the mass estimate. We have used the Mie theory to compute the extinction coefficient, which is exact only for spherical particles. For non-spherical particles, the extinction coefficient may differ from a Mie solution by a factor of 2 [*Liou*, 2002], which may introduce an additional uncertainty of $2^{1/3} = 1.26$ to the particle size estimate. Also, there is degeneracy between the two parameters describing the particle sizes. As suggested by equations (2)–(7), the mass of CO_2 condensates per unit volume indicated by certain MOLA channel depends on the product rG_1; and the key factor that determines the precipitation flux per unit area, $mv_{\rm F}$, depends on the product $r^3G_1G_2$. If the geometric factors can be constrained, the total mass of CO_2 condensation critically depends on the average particle radius to the power of 3, and consequently the particle radius may be accurately determined. So far we have been assuming $G_1 = 1$ and $G_2 = 1$, which is equivalent to the assumption that the condensate particles are monodisperse. In reality, the geometric factors may be larger than unity. Our estimates should therefore be regarded as upper limits of average condensate particle radii.

[74] The particle radius in the condensation cloud depends on all physical processes involved in the cloud formation, including nucleation, coagulation, condensational growth, precipitation, and dynamical transport [*Toon and Farlow*, 1981]. The competition between the timescales of these processes determines the average particle radius. *Glandorf et al.* [2002] estimate at 10 km the condensate particles have radii of 22 μm by assuming dust concentrations of 18 particles cm^{-3} and complete nucleation followed by rapid condensational growth until the saturation ratio reduces to unity, consistent with our estimates. As a result, nucleation and condensational growth can explain the particle size we find. Moreover, precipitation may be important for removing large particles and truncating the condensational growth. The precipitation timescale decreases with the particle radius, whereas the growth timescale increases with particle radius. If the precipitation is the key limit for the particle to grow, in equilibrium, the falling timescale should be comparable to the growth timescale. *Colaprete and Toon* [2003] investigated the formation of CO_2 clouds during Mars' polar nights considering microphysical processes including nucleation and condensational growth of a CO_2 ice particle. For Mars' 6.2 mbar atmosphere, the balance between sedimentation and condensational growth gives a radius of about 20 μm [*Colaprete and Toon*, 2003], which is consistent with our results. In summary, we find our estimates of particle radius to be 8–23 μm for the northern hemisphere and 4–13 μm for the southern hemisphere are sensible from the microphysical point of view.

[75] Previous numerical simulations of the Martian CO_2 condensation and cloud formation, however, suggest the condensate particles to be larger. *Colaprete and Toon* [2002] simulated the CO_2 snow storm during the Martian polar night considering the cloud microphysics and the mountain waves on Mars. The nucleating sizes are assumed to be dust particles of 5 μm. The simulation predicts that the average size of condensate particles that are being deposited to the surface is about 200 μm, much larger than our results. For the convective clouds, it is suggested that the particle radius most critically depends on the ice nuclei concentration and the updraft velocity [*Colaprete et al.*, 2003]. The updraft velocity is in turn a function of the available convective potential energy (CAPE) within the atmosphere. We do not find any association between the CAPE and the MOLA cloud opacities within our limited samples of saturation-condensate association events (section 3.1.2). Numerical simulations suggest that the typical particle radius of a convective cloud is 20–60 μm when extinction is comparable to MOLA channel 1 and 2 [*Colaprete et al.*, 2003]. The most recent and complete (from a physical processes standpoint) modeling by *Colaprete et al.* [2008] has CO_2 cloud particles area weighted radii around 60 μm in the north and 30 μm in the south, slightly larger than our estimates. The discrepancy between our particle size estimates and the MGCM model results may be due to the fact that MOLA only views the uppermost part of the clouds, where the smallest particles may be concentrated. For a convective CO_2 cloud in Mars' atmosphere, larger particles tend to be concentrated at lower altitudes and precipitate out rapidly [*Colaprete et al.*, 2003]. It is therefore not surprising that the column-integrated average particle radius from MGCM models is larger than our estimates.

[76] Our estimates indicate a putative north-south difference of the CO_2 condensate particle radius. The condensate particles in the northern hemisphere is estimated to be larger than in the southern hemisphere to compensate for much smaller atmospheric saturation area. The uncertainty ranges of northern hemisphere particle radius and southern hemisphere particle radius overlap. The north-south particle size difference can probably be explained by the fact that the atmosphere is thicker by almost one scale height in the northern hemisphere than in the southern hemisphere. The size difference is also consistent with the MGCM models [e.g., *Colaprete et al.*, 2008]. Finally, we emphasize that the particle size estimates in this paper is mostly relevant to the upper part of CO_2 clouds in Mars' polar regions, and may not be a suitable probe of the particle size of precipitating CO_2 or the grain size of surface CO_2 snow. Indeed, the cold spots in the northern hemisphere tend to have larger temperature differences between the TES 18 and 25 μm bands than those in the southern hemisphere, which may indicate that the grain size of CO_2 snow is larger in the southern hemisphere than in the northern hemisphere [*Cornwall and Titus*, 2010]. The connection between the grain size of surface snow and the particle size on the top of clouds remains to be investigated with the cloud microphysics.

5. Conclusion

[77] In this paper we study condensation of CO_2 in Mars' atmosphere and estimate the masses of CO_2 condensates deposited onto the seasonal polar caps in the northern and southern hemispheres. We analyze the temperature profiles retrieved from radio occultation measurements from MGS RS and the broad-band infrared spectroscopy of the MCS instrument. We also investigate non-ground returns from the MGS MOLA instrument. Based on the multi-instrument data analysis, we arrive at three main conclusions.

[78] 1. We provide causal evidence that MOLA non-ground returns are associated with condensation of atmospheric CO_2. We find 11 events in MY 24 in which a temperature profile measured by radio occultation of the MGS RS is geographically and seasonally associated with a number of MOLA non-ground returns. The reflective clouds are found to be within the condensation layer of CO_2. The association strongly indicates the MOLA non-ground returns to indicate particles in CO_2 clouds.

[79] 2. We reveal the seasonal variation of atmospheric saturation on Mars with the MCS data. We find that the area and thickness of atmospheric saturation expand from fall to winter and shrink from winter to spring. The area and the thickness of CO_2 condensation are both larger in the southern hemisphere than in the northern hemisphere. Atmospheric saturation in the northern hemisphere exhibits more intense seasonal and latitudinal variations.

[80] 3. We estimate the total mass of CO_2 that is condensed and deposited onto the seasonal polar caps in the northern and southern hemispheres, and infer the average particle radius of CO_2 condensates to be 8–22 μm in the north and 4–13 μm in the south. The area and the occurrence rate of atmospheric condensation as a function of season, or time, is determined from atmospheric temperature profiles measured by the MCS. The precipitation flux is approximated by the particle settling flux derived from the cloud opacities

measured by MOLA filter channels. The comparison between our estimates and the seasonal polar masses inferred from the Mars' gravity variation indicates the average particle radius. The seasonal polar masses are scaled by a factor of 0.1 to account for the contribution of atmospheric precipitation in the formation of seasonal polar caps.

[81] We also identify several notable phenomena:

[82] 1. During polar nights, the atmospheric temperature profiles below the condensation layer of CO_2 generally follow the moist adiabatic lapse rate in the southern hemisphere. The temperature gradient below the CO_2 condensation layer in northern hemisphere, however, is generally smaller than the moist adiabatic lapse rate.

[83] 2. The atmospheric saturation in the northern polar region feature temporal variation in occurrence rates near the low-latitude boundary of the seasonal cap, which may be due to the intense baroclinic wave activity in the northern mid-latitude region.

[84] 3. A planet-encircling dust storm in MY 28 suppressed condensation of CO_2 in the northern hemisphere, which led to a decrease of thickness of the CO_2 condensation layer, a shrinking of the area on where CO_2 condenses, and a decrease of the occurrence rate of atmospheric saturation.

[85] In summary, we derive the geographical and vertical extent of CO_2 condensation and the mass of condensates in Mars' atmosphere based on temperature profiles measured by MGS RS and MCS, and find condensation of CO_2 to be the cause of reflective clouds detected by MOLA and to contribute to the variation of seasonal polar cap masses. This work places new constraints on the Martian atmosphere that elucidate the annual cycle of CO_2 exchange.

Appendix A: Saturation Pressure of CO_2 and Moist Adiabatic Lapse Rate of Mars

[86] For each temperature profile measured by radio occultation, we compare its pressure levels (P) with the saturation pressure P_{sat}. If $P > P_{sat}$, the atmosphere is saturated and condensation may occur. P_{sat} depends on temperature (T) as

$$\log_{10}P_{sat} = 3.128082 - \frac{867.2124}{T} + 18.65612\times10^{-3}T - 72.48820\times10^{-6}T^2 + 93\times10^{-9}T^3 \quad \text{(A1)}$$

for $T > 216.56$ K and

$$\log_{10}P_{sat} = 6.760956 - \frac{1284.07}{T-4.718} + 1.256\times10^{-4}(T-143.15) \quad \text{(A2)}$$

for $T < 216.56$ K [*Vukalovich and Altunin*, 1968; *Kasting*, 1991].

[87] The moist adiabatic lapse rate is given by *Kasting* [1991] as:

$$\left(\frac{dP}{dT}\right)_{ad} = \rho C_P\left(\frac{1+\frac{81P_vL^2}{11000C_PPRT^2}}{1+\frac{18P_vL}{1000PRT}}\right), \quad \text{(A3)}$$

where ρ is the mass density of the atmosphere, P_v is the partial pressure of water vapor, L is the specific latent heat of sublimation of water for which we adopt $L = 2.27\times10^6\ \mathrm{J\,kg^{-1}}$ and C_P is the constant-pressure specific heat capacity of CO_2 [*Curry and Webster*, 1999]. For CO_2 as an ideal gas, C_P depends on temperature as

$$C_p(\mathrm{cal/mole}) = 7.7 + 5.3\times10^{-3}T - 8.3\times10^{-7}T^2. \quad \text{(A4)}$$

In the calculation of moist adiabatic lapse rate we assume a mixing ratio of water vapor of 10 parts per million by volume (ppmv) [e.g., *Krasnopolsky*, 2006]. The water content has a minor effect on the lapse rate. For example, a water vapor level of 10 ppmv only increases the adiabatic temperature-pressure gradient by 0.2% compared to a completely dry atmosphere.

Appendix B: Derivation of Geometric Factors

[88] We derive the mass of CO_2 condensate particles per unit volume indicated by certain MOLA filter channels and relevant geometric factors that describe the size distribution of particles.

[89] The lognormal size distribution of condensate particles is

$$n_N(\ln r_P) = \frac{n}{(2\pi)^{1/2}\ln\sigma_g}\exp\left(-\frac{(\ln r_P - \ln r)^2}{2\ln^2\sigma_g}\right), \quad \text{(B1)}$$

where n_N is the number of particles per unit volume per log-radius ($\ln r_P$), n is the total number of particle per unit volume, r is the average particle radius and σ_g is the geometric standard deviation defined as the ratio of radius below which 84.1% of the particles lie to the median radius [*Seinfeld and Pandis*, 2006].

[90] Based on the lognormal size distribution, the opacity of CO_2 clouds is

$$\begin{aligned} k &= \int_0^\infty F\pi r_P^2 n_N(\ln r_P)d\ln r_P \\ &= F\pi r^2 n\exp\left(2\ln^2\sigma_g\right) \\ &\equiv F\pi r^2 n G_2. \end{aligned} \quad \text{(B2)}$$

Here we have assumed that the Mie theory extinction factor F does not depend on particle radius, which is the case when the particle radius is much larger than the wavelength. The geometric factor G_2 is derived from the integration of lognormal size distribution multiplied by the polynomial r_P^2. This factor is therefore also applicable to the settling velocity in cases of $C_c \sim 1$, i.e., equation (6).

[91] The total mass of CO_2 condensate particles per unit volume is

$$\begin{aligned} m &= \int_0^\infty \rho\frac{4}{3}\pi r_P^3 n_N(\ln r_P)d\ln r_P \\ &= \rho\frac{4}{3}\pi r^3 n\exp\left(\frac{9}{2}\ln^2\sigma_g\right) \\ &\equiv \rho\frac{4}{3}\pi r^3 n G_3. \end{aligned} \quad \text{(B3)}$$

As a result we have

$$\frac{m}{k} = \frac{4r\rho}{3F}\frac{G_3}{G_2} \equiv \frac{4r\rho}{3F}G_1, \tag{B4}$$

which yields the equations (2) and (3).

[92] **Acknowledgments.** We thank Greg Neumann for providing MOLA non-ground return data, Peter Ford and Gordon Pettengill for insightful discussions about cloud formation on Mars, Tim Schofield and David Kass for discussions about the MCS data, Anthony Colaprete and Timothy Titus for careful review of the manuscript, and Francois Forget for discussions about the atmospheric condensation. This analysis was supported by the Radio Science Gravity investigation of the NASA Mars Reconnaissance Orbiter mission. RH was partly supported by the NASA Earth and Space Science Fellowship (NNX11AP47H).

References

Barnes, J. R., J. B. Pollack, R. M. Haberle, C. B. Leovy, R. W. Zurek, H. Lee, and J. Schaeffer (1993), Mars atmospheric dynamics as simulated by the NASA Ames general circulation model: 2. Transient baroclinic eddies, *J. Geophys. Res.*, *98*, 3125–3148, doi:10.1029/92JE02935.

Clancy, R., B. Sandor, M. Wolff, P. Christensen, M. Smith, J. Pearl, B. Conrath, and R. Wilson (2000), An intercomparison of ground-based millimeter, MGS TES, and Viking atmospheric temperature measurements: Seasonal and interannual variability of temperatures and dust loading in the global Mars atmosphere, *J. Geophys. Res.*, *105*, 9553–9571, doi:10.1029/1999JE001089.

Colaprete, A., and O. B. Toon (2002), Carbon dioxide snow storms during the polar night on Mars, *J. Geophys. Res.*, *107*(E7), 5051, doi:10.1029/2001JE001758.

Colaprete, A., and O. B. Toon (2003), Carbon dioxide clouds in an early dense Martian atmosphere, *J. Geophys. Res.*, *108*(E4), 5025, doi:10.1029/2002JE001967.

Colaprete, A., R. M. Haberle, and O. B. Toon (2003), Formation of convective carbon dioxide clouds near the south pole of Mars, *J. Geophys. Res.*, *108*(E7), 5081, doi:10.1029/2003JE002053.

Colaprete, A. R., J. R. Barnes, R. M. Haberle, J. L. Hollingsworth, H. H. Kieffer, and T. N. Titus (2005), Albedo of the south pole on Mars determined by topographic forcing of atmospheric dynamics, *Nature*, *435*, 184–188.

Colaprete, A., R. B. Jeffrey, R. M. Haberle, and F. Montmessin (2008), CO_2 clouds, CAPE ad convection on Mars: Observations and general circulation modeling, *Planet. Space Sci.*, *56*, 150–180.

Conrath, B. J., J. C. Pearl, M. D. Smith, W. C. Maguire, P. R. Christensen, S. Dason, and M. S. Kaelberer (2000), Mars Global Surveyor Thermal Emission Spectrometer (TES) observations: Atmospheric temperatures during aerobraking and science phasing, *J. Geophys. Res.*, *105*, 9509–9519, doi:10.1029/1999JE001095.

Cornwall, C., and T. N. Titus (2009), Spatial and temporal distributions of Martian north polar cold spots before, during, and after the global dust storm of 2001, *J. Geophys. Res.*, *114*, E02003, doi 10.1029/2008JE003243.

Cornwall, C., and T. N. Titus (2010), A comparison of Martian north and south polar cold spots and the long-term effects of the 2001 global dust storm, *J. Geophys. Res.*, *115*, E06011, doi:10.1029/2009JE003514.

Curry, J. A., and P. J. Webster (1999), *Thermodynamics of Atmospheres and Oceans*, Acad. Press, London.

Forget, F., and J. B. Pollack (1996), Thermal infrared observations of the condensing Martian polar caps: CO_2 ice temperatures and radiative budget, *J. Geophys. Res.*, *101*, 16,865–16,879, doi:10.1029/96JE01077.

Forget, F., G. B. Hansen, and J. B. Pollack (1995), Low brightness temperatures of Martian polar caps: CO_2 clouds or low surface emissivity?, *J. Geophys. Res.*, *100*, 21,219–21,234, doi:10.1029/95JE02378.

Forget, F., F. Hourdin, and O. Talagrand (1998), CO_2 snowfall on Mars: Simulation with a general circulation model, *Icarus*, *131*, 302–316.

Glandorf, D. L., A. Colaprete, and M. A. Tolbert (2002), CO_2 snow on Mars and early Earth: Experimental constraints, *Icarus*, *160*, 66–72.

Haberle, R. M., F. Forget, A. Colaprete, J. Schaeffer, W. V. Boynton, N. J. Kelly, and M. A. Chamberlain (2008), The effect of ground ice on the Martian seasonal CO_2 cycle, *Planet. Space Sci.*, *56*, 251–255.

Hansen, G. B. (1999), Control of the radiative behavior of the Martian polar caps by surface CO_2 ice: Evidence from Mars Global Surveyor measurements, *J. Geophys. Res.*, *104*, 16,471–16,486, doi:10.1029/1998JE000626.

Heavens, N. G., D. J. McCleese, M. I. Richardson, D. M. Kass, A. Kleinböhl, and J. T. Schofield (2011), Structure and dynamics of the Martian lower and middle atmosphere as observed by the Mars Climate Sounder: 2. Implications of the thermal structure and aerosol distributions for the mean meridional circulation, *J. Geophys. Res.*, *116*, E01010, doi:10.1029/2010JE003713.

Hess, S. L., R. M. Henry, and J. E. Tillman (1979), The seasonal variation of atmospheric pressure on Mars as affected by the south polar cap, *J. Geophys. Res.*, *84*, 2923–2927, doi:10.1029/JB084iB06p02923.

Hinson, D. P. (2006), Radio occultation measurements of transient eddies in the northern hemisphere of Mars, *J. Geophys. Res.*, *111*, E05002, doi:10.1029/2005JE002612.

Hinson, D. P., R. A. Simpson, J. D. Twicken, G. L. Tyler, and F. M. Flasar (1999), Initial results from radio occultation measurements with Mars Global Surveyor, *J. Geophys. Res.*, *104*, 26,997–27,012, doi:10.1029/1999JE001069.

Hunt, G. E. (1980), On the infrared radiative properties of CO_2 ice clouds: Application to Mars, *Geophys. Res. Lett.*, *7*, 481–484, doi:10.1029/GL007i007p00481.

Iraci, L. T., B. D. Phebus, B. M. Stone, and A. Colaprete (2010), Water ice cloud formation on Mars is more difficult than presumed: Laboratory studies of ice nucleation on surrogate materials, *Icarus*, *210*, 985–991.

Ivanov, A. B., and D. O. Muhleman (2001), Cloud reflection observations: Results from the Mars Orbiter Laser Altimeter, *Icarus*, *154*, 190–206.

Kasting, J. M. (1991), CO_2 condensation and the climate of early Mars, *Icarus*, *94*, 1.

Kieffer, H. H., and T. N. Titus (2001), TES mapping of Mars' north seasonal cap, *Icarus*, *154*, 162.

Kieffer, H. H., T. Z. Martin, S. C. Chase, E. D. Miner, F. D. Palluconi, G. Muench, and G. Neugebauer (1976), Infrared thermal mapping of the Martian surface and atmosphere: First results, *Science*, *193*, 780–786.

Kieffer, H., T. Titus, K. Mullins, and P. Christensen (2000), Mars south polar spring and summer behavior observed by TES: Seasonal cap evolution controlled by frost grain size, *J. Geophys. Res.*, *105*, 9653–9699, doi:10.1029/1999JE001136.

Kleinböhl, A., et al. (2009), Mars Climate Sounder limb profile retrieval of atmospheric temperature, pressure, and dust and water ice opacity, *J. Geophys. Res.*, *114*, E10006, doi:10.1029/2009JE003358.

Krasnopolsky, V. A. (2006), Photochemistry of the martian atmosphere: Seasonal, latitudinal, and diurnal variations, *Icarus*, *185*, 153.

Kuroda, T., A. S. Medvedev, P. Hartogh, and M. Takahashi (2007), Seasonal changes of the baroclinic wave activity in the northern hemisphere of Mars simulated with a GCM, *Geophys. Res. Lett.*, *34*, L09203, doi:10.1029/2006GL028816.

Langevin, Y., J.-P. Bibring, F. Montmessin, F. Forget, M. Vincendon, S. Douté, F. Poulet, and B. Gondet (2007), Observations of the south seasonal cap of Mars during recession in 2004–2006 by the OMEGA visible/near-infrared imaging spectrometer on board Mars Express, *J. Geophys. Res.*, *112*, E08S12, doi:10.1029/2006JE002841.

Leighton, R. B., and B. C. Murray (1966), Behavior of carbon Dioxide and other volatiles on Mars, *Science*, *153*, 136–144.

Liou, K. N. (2002), *An Introduction to Atmospheric Radiation*, 2nd ed., Acad. Press, San Diego, Calif.

Litvak, M. L., I. G. Mitrofanov, A. S. Kozyrev, A. B. Sanin, V. I. Tretyakov, W. V. Boynton, D. Hamara, C. Shinohara, and R. S. Saunders (2005), Modeling of Martian seasonal caps from HEND/ODYSSEY data, *Adv. Space Res.*, *36*, 2156–2161.

Litvak, M. L., I. G. Mitrofanov, A. S. Kozyrev, A. B. Sanin, V. I. Tretyakov, W. V. Boynton, N. J. Kelly, D. Hamara, and R. S. Saunders (2007), Long-term observations of southern winters on Mars: Estimations of column thickness, mass, and volume density of the seasonal CO_2 deposit from HEND/Odyssey data, *J. Geophys. Res.*, *112*, E03S13, doi:10.1029/2006JE002832.

McCleese, D. J., J. T. Schofield, F. W. Taylor, S. B. Calcutt, M. C. Foote, D. M. Kass, C. B. Leovy, D. A. Paige, P. L. Read, and R. W. Zurek (2007), Mars Climate Sounder: An investigation of thermal and water vapor structure, dust and condensate distributions in the atmosphere, and energy balance of the polar regions, *J. Geophys. Res.*, *112*, E05S06, doi:10.1029/2006JE002790.

McCleese, D. J., et al. (2010), Structure and dynamics of the Martian lower and middle atmosphere as observed by the Mars Climate Sounder: Seasonal variations in zonal mean temperature, dust and water ice aerosols, *J. Geophys. Res.*, *115*, E12016, doi:10.1029/2010JE003677.

Montmessin, F., et al. (2006), Subvisible CO_2 ice clouds detected in the mesosphere of Mars, *Icarus*, *183*, 403.

Neumann, G. A., D. E. Smith, and M. T. Zuber (2003), Two Mars years of clouds detected by the Mars Orbiter Laser Altimeter, *J. Geophys. Res.*, *108*(E4), 5023, doi:10.1029/2002JE001849.

Pettengill, G. H., and P. G. Ford (2000), Winter clouds over the north Martian polar cap, *Geophys. Res. Lett.*, *27*, 609–612, doi:10.1029/1999GL010896.

Pollack, J., R. Haberle, J. Schaeffer, and H. Lee (1990), Simulations of the general circulation of the Martian atmosphere: 1. Polar processes, *J. Geophys. Res.*, *95*, 1447–1473, doi:10.1029/JB095iB02p01447.

Pollack, J., R. Haberle, J. Murphy, J. Schaeffer, and H. Lee (1993), Simulations of the general circulation of the Martian atmosphere: 2. Seasonal pressure variations, *J. Geophys. Res.*, *98*, 3149–3181, doi:10.1029/92JE02947.

Putzig, N. E., and M. T. Mellon (2007), Apparent thermal inertia and the surface heterogeneity of Mars, *Icarus*, *191*, 68–94.

Rogers, R. R., and Yau, M. K. (1989), *A Short Course in Cloud Physics*, 3rd ed., Butterworth-Heinemann, Woburn, Mass.

Seinfeld, J. H., and S. N. Pandis (2006), *Atmospheric Chemistry and Physics – From Air Pollution to Climate Change*, 2nd ed., Wiley, Hoboken, N. J.

Smith, D. E., M. T. Zuber, and G. A. Newmann (2001a), Seasonal variation of snow depth on Mars, *Science*, *294*, 2141–2146.

Smith, D. E., et al. (2001b), Mars Obiter Laser Altimeter: Experiment summary after the first year of global mapping of Mars, *J. Geophys. Res.*, *106*, 23,689–23,722, doi:10.1029/2000JE001364.

Smith, M. D., M. J. Wolff, R. T. Clancy, and S. L. Murchie (2009a), Compact Reconnaissance Imaging Spectrometer observations of water vapor and carbon monoxide, *J. Geophys. Res.*, *114*, E00D03, doi:10.1029/2008JE003288.

Smith, D. E., M. T. Zuber, M. H. Torrence, P. J. Dunn, G. A. Neumann, F. G. Lemoine, and S. K. Fricke (2009b), Time variations of Mars' gravitational field and seasonal changes in the masses of the polar ice caps, *J. Geophys. Res.*, *114*, E05002, doi:10.1029/2008JE003267.

Spiga, A., F. González-Galindo, M.-A. Lopez-Valverde, and F. Forget (2012), Gravity waves, cold pockets and CO_2 clouds in the Martian mesosphere, *Geophys. Res. Lett.*, *39*, L02201, doi:10.1029/2011GL050343.

Thomas, P. C., P. B. James, W. M. Calvin, R. Haberle, and M. C. Malin (2009), Residual south polar cap of Mars: Stratigraphy, history, and implications of recent changes, *Int. J. Sol. Syst. Stud.*, *203*, 352–375.

Tillman, J. E., N. C. Johnson, P. Guttorp, and D. B. Percival (1993), The Martian annual atmospheric pressure cycle: Years without great dust storms, *J. Geophys. Res.*, *98*, 10,963–10,971, doi:10.1029/93JE01084.

Titus, T. N., H. H. Kieffer, K. F. Mullins, and P. R. Christensen (2001), TES premapping data: Slab ice and snow flurries in the Martian north polar night, *J. Geophys. Res.*, *106*, 23,181–23,196, doi:10.1029/2000JE001284.

Tobie, G., F. Forget, and F. Lott (2003), Numerical simulation of the winter polar wave clouds observed by Mars Global Surveyor Mars Orbiter Laser Altimeter, *Icarus*, *164*, 33–49.

Toon, O. B., and N. H. Farlow (1981), Particles above the tropopause, Measurements and models of stratospheric aerosols, meteoric debris, nacreous clouds, and noctilucent clouds, *Annu. Rev. Earth. Planet. Sci.*, *9*, 19–58.

Tyler, G., G. Balmino, D. Hinson, W. Sjogren, D. Smith, R. Woo, S. Asmar, M. Connally, C. Hamilton, and R. Simpson (1992), Radio science investigations with Mars Observer, *J. Geophys. Res.*, *97*, 7759–7779, doi:10.1029/92JE00513.

Tyler, G., G. Balmino, D. Hinson, W. Sjogren, D. Smith, R. Simpson, S. Asmar, P. Priest, and J. Twicken (2001), Radio Science observations with Mars Global Surveyor: Orbit insertion through one Mars year in mapping orbit, *J. Geophys. Res.*, *106*, 23,327–23,348, doi:10.1029/2000JE001348.

Vukalovich, M. P., and V. V. Altunin (1968), *Thermophysical Properties of Carbon Dioxide*, Collet's Publ., London.

Wagstaff, K. L., T. N. Titus, A. B. Ivanov, R. Castano, and J. L. Bandfield (2008), Observations of the north polar water ice annulus on Mars using THEMIS and TES, *Planet. Space Sci.*, *56*, 256–265.

Warren, S. G. (1996), Optical constants of carbon dioxide ice, *Appl. Opt.*, *25*, 2650–2674.

Wood, S. E., and D. A. Paige (1992), Modeling the Martian seasonal CO_2 cycle: 1. Fitting the Viking Lander pressure curves, *Icarus*, *99*, 1–14.

Zuber, M. T., D. Smith, S. Solomon, D. Muhleman, J. Head, J. Garvin, J. Abshire, and J. Bufton (1992), The Mars Observer Laser Altimeter investigation, *J. Geophys. Res.*, *97*, 7781–7797, doi:10.1029/92JE00341.

Zuber, M. T., et al. (1998), Observations of the north polar region of Mars from the Mars Orbiter Laser Altimeter, *Science*, *282*, 2053–2060.

Zurek, R. W. (1992), Comparative aspects of the climate of Mars: An introduction to the current atmosphere, in *Mars*, edited by H. H. Kieffer et al., pp. 799–817, Univ. of Ariz. Press, Tucson.

Zurek, R. W., and S. E. Smrekar (2007), An overview of the Mars Reconnaissance Orbiter (MRO) science mission, *J. Geophys. Res.*, *112*, E05S01, doi:10.1029/2006JE002701.